Article

ANN-Based Model for the Prediction of the Bond Strength between FRP and Concrete

Alessio Cascardi [1,*] **and Francesco Micelli** [2]

1   ITC-CNR, Construction Technologies Institute, Italian National Research Council, 70124 Bari, Italy
2   Department of Innovation Engineering, University of Salento, Via per Monteroni, 73100 Lecce, Italy; francesco.micelli@unisalento.it
*   Correspondence: alessio.cascardi@itc.cnr.it

Abstract: In the last decades, the uses of fiber reinforced polymer (FRP) composites in the structural strengthening of reinforced concrete (RC) structures have become the state of the art, providing a valid alternative to the traditional use of steel plates. These relatively new materials present, in fact, great advantages, including high corrosion resistance in aggressive environments, low specific weight, high strength-to-mass-density ratio, magnetic and electric neutrality, low axial coefficient of thermal expansion and sustainable costs of installation. In flexural and shear strengthening of RC members, the effectiveness of the epoxy bonded FRP strongly depends on the adhesion forces exchanged with the concrete substrate. When the flexural moment is present, the FRP strengthening is activated through the stress transfer on the tension side, which is guaranteed by the contact beam region to which the adhesive is bonded to the beam itself. Hence, the determination of the maximum forces that cause debonding of the FRP-plate becomes crucial for a proper design. Over the years, many different analytical models have been provided in the scientific literature. Most of them are based on the calibration of the narrow experimental database. Now, hundreds of experimental results are available. The main goal of the current study is to present and discuss an alternative theoretical formulation for predicting the debonding force in an FRP-plate, epoxy-bonded to the concrete substrate by using an artificial neural networks (ANNs) approach. For this purpose, an extensive study of the state of the art, reporting the results of single lap shear tests, is also reported and discussed. The robustness of the proposed analytical model was validated by performing a parametric analysis and a comparison with other existing models and international design codes, as shown herein.

Keywords: artificial neural networks; FRP; bond; strengthening; RC beam

1. Introduction

The existing reinforced concrete (RC) structures have been demonstrated to suffer extensive damage during seismic events [1–3]. In these cases, externally bonded reinforcements (EBR) in the forms of FRPs may represent a quick and suitable solution for the structural rehabilitation also because they can be applied in pre-stressed action. The knowledge on the bond behavior at the interface between the FRP and the concrete substrate is essential in order to provide a proper design of the FRP-strengthening. Bond performance between FRP and concrete has been widely studied either experimentally by using the pull-off tests, by calibrating theoretical models and by using finite element model (FEM), e.g., in [4–19]. The prediction of the ultimate tensile force that can be carried by an FRP plate in a simple pull-off test, before the debonding failure, has been the main target of these studies. Typically, concrete prisms are used, and a tensile force is applied (parallel to the longitudinal direction of the fibers) to the FRP to measure the ultimate load (P_u) which allows computation of the bond strength in terms of ultimate tangential stresses (τ_f).

The available research in the field (e.g., in [10–19]) has conclusively shown that the ultimate delamination load initially increases by increasing the bond length, but over a

threshold value, any further increase in the bond length does not lead to a further increment of in the ultimate load. Therefore, it is well-known that only a part of the bond length is mobilized in resisting the ultimate load. The mentioned threshold value of the bond length is commonly referred to the active or effective bond length as reported in [18], which represents the length actively involved in the force transfer between the FRP strip and the concrete. The purpose of this research is to provide a new relationship for predicting the delamination load (P_u), calibrated by using an artificial neural networks (ANN) method, between an FRP plate and a concrete rigid substrate. It should be evidenced that the proposed formulation is based on an up-dated large database, analyzed by a modern and well recognized data-mining technique, such as the ANN. In this context a previous attempt was found in [20], where a database of fifty-nine experimental tests of FRP-strengthened specimens was used to study the debonding failure. Starting from that analysis, the present work aims to assess a new ANN predictive model, based on an updated database made up of more than 350 samples, tested in the single lap shear test configurations. In summary, the result consists in the calibration of relationships able to predict the ultimate delamination force P_u. The main goal is to perform a novel analytical expression which may answer to the requirement of improved simplicity and accuracy with respect to the available analytical models as demonstrated in the next sections.

2. A Background of the Bond Behavior between FRP and Concrete Substrate

It has been highlighted that the interfacial bond between FRP and concrete plays a crucial role in maintaining the mechanical performance and the durability of FRP-strengthened concrete structures. In the absence of specific standards, the recommendations reported in [21] are commonly recognized in relation to the bond test on an FRP strip/plate epoxy bonded to a rigid concrete block. The term rigid indicates that internal strains within the concrete block are neglected in the mechanical problem. Typically, the concrete support is fixed and an FRP strip/plate is externally bonded on it (see Figure 1) by using a manual procedure and an epoxy adhesive. A tensile force P is applied on the free side of the plate in the direction of the fibers. The force is increased until the delamination is reached, and the corresponding ultimate value of the load P_u is measured. The failure will occur along the weakest plane of the system: the FRP laminate, the adhesive or the substrate. In fact, three different failure modes have been commonly recognized (excluding the tensile breakage of the FRP itself): a concrete cover delamination, for which the concrete thickness is detached by remaining bonded to the FRP; an adhesive failure in which failure occurs within the resin (in this case the concrete substrate remains un-cracked) and a mixed fracture, namely both cohesive and adhesive. Referring to the Figure 1, the FRP strip/plate transmits the tensile force to the concrete through the tangential stresses τ_f, which arise at the interfaces. These stresses are not uniformly distributed since they are maximum at the loaded end, and decrease along the reinforcement, according to [13] and early in [22,23]. Based on non-linear fracture mechanics, the interfacial energy Gf is computed as the area below the bond stress–slip curve.

An extensive study on the analytical modeling of the FRP-concrete bond strength was conducted and the analyzed papers are listed in [22–34], while all the proposed formulations are resumed in Table 1. The models are chronologically arranged in order to show the evolution of the different approaches. The first effort in 1980 was made by Van Gemert [22]. The delamination load of an epoxy-bonded steel plate to a concrete substrate was expressed as the resultant of shear stresses, having a linear trend over the bond area. The maximum shear stress was related to the tensile strength of the concrete substrate. The analytical relationship was so-calibrated on the basis of the experimental results obtained by the authors and similar proposals can be found in [23] (Ph.D. thesis) and [28–34] (for FRP-plate). An energetic approach was primarily proposed in a scientific paper by Neidermeier in [28]; which considered the fracture energy, G_f, and the role of the effective bond length. This last work inspired more recent studies, such as those reported in [33–37]. Most of the proposed relationships to determine the bond strength consist in a

piecewise defined function (see [28–30,34–36,38–40]) depending on the anchorage length of the FRP sheet. In 1997 Maeda et al. [26] developed an empirical model in which, for the first time, a value of the effective bond length is proposed as a function of the properties of the FRP. Khalifa et al. [27] modified Maeda et al. model by including the concrete compressive strength, when evaluating the maximum bond stress (τ_a). The reported formulations are applicable to both hand lay-up and prefabricated FRP-systems bonded to concrete substrates. It can be noticed that most of the models in Table 1 refers to an empirical calibration. Commonly, the experimental relationship between the bond shear stress and the distance from the applied force point was experienced non-linear (generally hyperbolic or trigonometric shape). In addition, the geometrical and the mechanical properties are generally considered by introducing them as dimensionless.
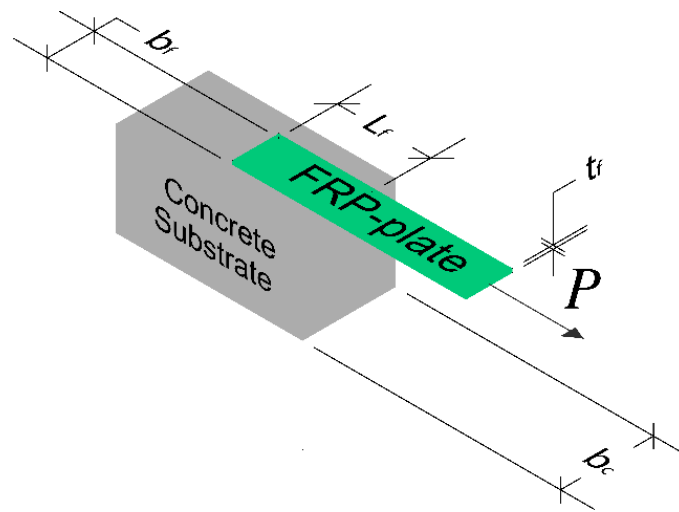
Figure 1. Sketch of the pull-pull shear test setup.

Table 1. Analytical models for the prediction of the bond strength between FRP and concrete.

Reference	Year	Model	Description
[22]	1980	$P_u = 0.5 b_f L f_{ctm}$	Based on an assumed triangular bond-stress distribution.
[23]	1994	$P_u = b_f \sqrt{E_f t_f G_f}$ where: $G_f = c_f f_{ctm}$ with $c_f = 0.204$ mm	Introduction of the fracture energy in a Ph.D thesis.
[24]	1996	$P_u = \tau_a b_f L$ where: $\tau_a = 6.13 - lnL$	Analytical linear interpretation of the bond-stress based on experimental data.
[25]	1997	$P_u = \tau_a b_f L$ where: $\tau_a = 5.88 L^{-0.669}$	Analysis of debonding in RC members strengthened with FRP.
[26]	1997	$P_u = \tau_a b_f L_e$ where: $L_e = e^{[6.13 - 0.58 ln(E_f t_f)]}$ $\tau_a = 110.2 \times 10^{-6} E_f t_f$	First definition of the effective bond length calibrated with non-linear regression analysis based on experimental data. A linear bond-stress distribution is assumed.

Table 1. *Cont.*

Reference	Year	Model	Description
[27]	1998	$P_u = \tau_a b_f L_e$ where: $L_e = e^{[6.13 - 0.58 ln(E_f t_f)]}$ $\tau_a = 110.2 \times 10^{-6} E_f t_f \left(\frac{f_c}{42}\right)^{2/3}$	Effective bond length calibration with non-linear regression analysis based on experimental data. Non-linear bond-stress distribution is assumed
[28]	2000	$P_u = \begin{cases} 0.78 b_f \sqrt{E_f t_f G_f} & se\ L \geq L_e \\ 0.78 b_f \sqrt{E_f t_f G_f}\ \frac{L}{L_e}\left(2 - \frac{L}{L_e}\right) & se\ L < L_e \end{cases}$ where: $L_e = \sqrt{\frac{E_f t_f}{4 f_{ctm}}}$ $G_f = c_f f_{ctm} \beta_w^2$ $\beta_w = \sqrt{1.125\left(\frac{2 - b_f/b_c}{1 + b_f/400}\right)}$	Introduction of the geometrical factor related to the width of the bonded plate and the width of the concrete member.
[29]	2001	$P_u = \begin{cases} 0.427 \beta_w b_f L_e \sqrt{f_c} & se\ L \geq L_e \\ 0.427 \beta_w b_f L_e \sqrt{f_c}\ \sin\left(\frac{\pi L}{2 L_e}\right) & se\ L < L_e \end{cases}$ where: $L_e = \sqrt{\frac{E_f t_f}{\sqrt{f_c}}}$ $\beta_w = \sqrt{\frac{2 - b_f/b_c}{1 + b_f/b_c}}$	A modified version of the model reported in [23], validated for both CFRP and steel plates. The shear-slip relationship is represented by a triangular shape.
[30]	2001	$P_u = \begin{cases} 0.64 \alpha \beta_w b_f k_c \sqrt{E_f t_f f_{ctm}} & se\ L \geq L_e \\ 0.64 \alpha \beta_w b_f k_c \sqrt{E_f t_f f_{ctm}}\ \frac{L}{L_e}\left(2 - \frac{L}{L_e}\right) & se\ L < L_e \end{cases}$ where: $\beta_w = 1.06 \sqrt{\frac{2 - b_f/b_c}{1 + b_f/400}}$ $L_e = \sqrt{\frac{E_f t_f}{2 f_{ctm}}}$ with $\alpha = 1$ and $kc = 1$.	International code based on the proposals from [27,28].
[31]	2001	$P_u = \left(0.5 + 0.08\sqrt{\frac{E_f t_f}{100 f_{ctm}}}\right) \tau_a b_f L_e$ where: $\tau_a = 0.5 f_{ctm}$ $Le = 100\ mm$	The effective bond length has been considered not affected by the compressive strength of the substrate and fixed to 100 mm based on authors experimentations. An empirical model has been calibrated.
[32]	2003	$P_u = \tau_a b_f L_e$ where: $L_e = 0.125\left(E_f t_f\right)^{0.57}$ $\tau_a = 0.93 f_c^{0.44}$	Simplified empirical model based on literature database. A non-linear bond-stress distribution, along the FRP-length, has been assumed.
[33]	2004	$P_u = b_f \sqrt{2 E_f t_f G_f} = b_f \sqrt{2 \frac{f_{ctm}}{8} E_f t_f} = 0.5 b_f \sqrt{E_f t_f f_{ctm}}$ where: $G_f = \frac{f_{ctm}}{8}$	Further empirical model based on literature database.
[34]	2005	$P_u = \begin{cases} b_f \sqrt{2 E_f t_f G_f} & se\ b_f < 100\ mm \\ \left(b_f + 2\Delta b_f\right)\sqrt{2 E_f t_f G_f} & se\ b_f \geq 100\ mm \end{cases}$ where: $G_f = 0.514 f_c^{0.236}$ $\Delta b_f = 3.7\ mm$	Analytical model for defining the nonlinear bond stress–slip law by means of non-linear regression analysis (authors data consisting in 26 tests).

Table 1. *Cont.*

Reference	Year	Model	Description
[35]	2005	$P_u = \beta_l b_f \sqrt{2 E_f t_f G_f}$ where: $\beta_l = \begin{cases} 1 & se\ L \geq L_e \\ \frac{L}{L_e}\left(2 - \frac{L}{L_e}\right) & se\ L < L_e \end{cases}$ $L_e = a + \frac{1}{2\lambda_1} ln\left[\frac{\lambda_1 + \lambda_2 tg(\lambda_2 a)}{\lambda_1 - \lambda_2 tg(\lambda_2 a)}\right]$ $G_f = 0.308 \beta_w^2 \sqrt{f_{ctm}}$ $\lambda_1 = \sqrt{\frac{\lambda_{max}}{s_o E_f t_f}}$ $\lambda_2 = \sqrt{\frac{\lambda_{max}}{(s_f - s_o) E_f t_f}}$ $\lambda_{max} = 1.5 \beta_w f_{ctm}$ $s_o = 0.0195 \beta_w f_{ctm}$ $s_f = \frac{2 G_f}{\lambda_{max}}$ $\beta_w = \sqrt{\frac{2.25 - b_f/b_c}{1.25 + b_f/b_c}}$	A linear best-fit line between finite element predictions, data collected from the existing literature (253 tests) and theoretical outcomes has been proposed by regression analysis.
[36]	2009	$P_u = \begin{cases} 0.585 b_f \beta_w f_c^{0.1} \left(E_f t_f\right)^{0.54} & se\ L \geq L_e \\ 0.585 b_f \beta_w f_c^{0.1} \left(E_f t_f\right)^{0.54} \left(\frac{L}{L_e}\right)^{1.2} & se\ L < L_e \end{cases}$ where: $\beta_w = \sqrt{\frac{2.25 - b_f/b_c}{1.25 + b_f/b_c}}$ $L_e = \frac{0.395 \left(E_f t_f\right)^{0.54}}{f_c^{0.09}}$	A bond strength model has been calibrated in order to reach an empirical formulation from the analysis of about 311 experimental data.
[37]	2010	$P_u = \beta_w b_f \sqrt{2 \left(1 + \frac{\lambda'}{\Sigma}\right) E_f t_f G_{cf}}$ where: $\beta_w = \sqrt{\frac{2 - b_f/b_c}{1 + b_f/b_c}}$ $\lambda' = \frac{t_d}{t_f}$ with t_d = 3.5 mm $\Sigma = \frac{E_f}{E_c}$ G_{cf} = 0.17 N/mm	A finite element analysis has been performed to determine the fracture energy.
[38]	2012	$P_u = 0.5 b_f \beta_w \sqrt{E_f t_f f_{ctm}}$ where: $\beta_w = 1.06 \sqrt{\frac{2 - b_f/b_c}{1 + b_f/400}}$	Simplified model calibrated by existing literature. It indicates that limiting the longitudinal shear stress (at the ultimate limit state) to a value not greater than 0.8 MPa, premature peeling failure can be avoided. It is further recommended that a minimum anchorage length of 500 mm should be provided.
[39]	2013	$P_u = \begin{cases} \frac{b_f}{\gamma_{Fd}} \sqrt{2 E_f t_f K_G \beta_w \sqrt{f_c f_{ctm}}} & se\ L \geq L_e \\ \frac{b_f}{\gamma_{Fd}} \sqrt{2 E_f t_f K_G \beta_w \sqrt{f_c f_{ctm}}} \frac{L}{L_e}\left(2 - \frac{L}{L_e}\right) & se\ L < L_e \end{cases}$ where: $L_e = max\left\{\frac{1}{\gamma_{Rd} f_{bd}} \sqrt{\frac{\pi^2 E_f t_f K_G \beta_w \sqrt{f_c f_{ctm}}}{2}}\ ;\ 200\ mm\right\}$ $\beta_w = \sqrt{\frac{2 - b_f/b_c}{1 + b_f/b_c}}.\ se\ b_f/b_c < 0.25$ $\gamma_{Rd} = 1.25$ $f_{bd} = \frac{2 \Gamma_{Fd}}{s_u}$ with su = 0.25 mm $\Gamma_{Fd} = K_G \beta_w \sqrt{f_c f_{ctm}}$ with $\gamma_{Fd} = 1.25$	Empirical model derived from available data and based on the evaluation of the specific fracture energy—Γ_{Fd}.

3. The Artificial Neural Networks (ANN)

Artificial neural networks (ANN) is a method for discovering useful patterns and trends in relatively large data-set. A network represents the joint probability models among given parameters (weight). Each variable is inputted in the system, and it is represented by a node in a graph (usually a tree scheme). The system is made up of an input layer, several hidden layers (chosen by the users) and an output layer.

The dependence between variables is indicated by direct links among the corresponding nodes and the conditional probabilities for each variable (hidden layer). The probability is conditioned (usually with an imposed bias) based on the possible combinations of values for the predecessors in the network. The information about the target is propagated through the network in a step-by-step updating of the probability distribution. The safe-scatter path is the ones which more accurately predict the desiderate output variable (i.e., target) by means of a transforming function. An analytical model is the result of this procedure adapted to extract information (namely "make knowledge") from data for forecasting the outcomes. An example of the above-described network is schematized in Figure 2.
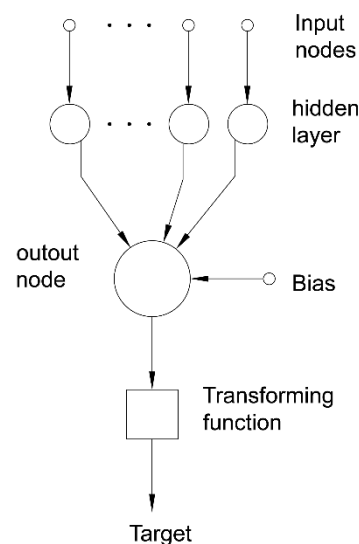
Figure 2. Artificial neural networks scheme example.

The ANN has been adopted and described exhaustively in the literature, e.g., in [40–46]. So, the fundamentals were only considered briefly in this paper. The most widely used ANN technique in civil engineering applications is the back-propagation networks (or B-ANN). The data flow from the input node to the output crossing a series of assumed hidden layer in which intermediate nodes are present in order to elaborate the inputs and make decisions related to the imposed bias. On the other hand, the error propagates in the opposite direction (from the computed output node to the inputs). In the propagation flow the weight and the bias are updated until the theoretical versus experimental scatter reaches a certain tolerance (small enough). The output node is then transformed by a non-linear function in the target, which is the outcome that the user is intended to predict. The relationships between the inputs and the outputs and the transforming function are typically written as reported in Equations (1) and (2), respectively.

$$y = b + \sum_{i=1}^{n} w_i \cdot x_i \tag{1}$$

$$T = \frac{1}{1 + e^{-ky}} \tag{2}$$

where:

- x_i is the input data of the generic i-input-node;
- w_i is the weight of a generic node in the hidden layer;
- b is the bias;
- y is the value of the output node;
- T is the target;
- K is a shape factor.

4. Experimental Database for the Formulation of the Theoretical Model

The collection of a wide database related to the results of the single lap shear test on FRP plate/strips and concrete substrate has been analyzed for the definition of an ANN analytical model able to estimate the bond strength. The collected results are extracted from several experimental studies, i.e., [47–64], by considering a single layer of carbon or glass FRP bonded on concrete blocks. The experimental results used as references for the implementation of the ANN model are reported in the Appendix A (Table A1). The main parameters considered for the analysis are the following:

- t_f, the thickness of the FRP sheet (mm);
- b_f, the width of the FRP sheet (mm);
- E_f, the Young's modulus of the FRP sheet (GPa);
- L_f, the bond length of the FRP sheet (mm);
- f_c, the compressive strength of the concrete (MPa);
- b_c, the width of the tested concrete element (mm).

In the case of FRP-sheets the term t_f is referred to the thickness of the dry fiber unidirectional sheet, in the case of pultruded plates t_f is the total thickness of the FRP plate. The ultimate force P_u (kN), namely the bond strength, was imposed as the target of the analysis.

In the database, different typologies of specimens are considered, such as sheet, plate, laminate and in situ cured FRP. The considered parameters have been normalized with respect to the corresponding maximum value and the relative frequency distribution has been computed and reported in the box-plot graphs of the Figure 3. In addition, the interquartile range—IQR (i.e., the difference between the third and the first quartile)—is illustrated in Table 2 for each studied property. It is clear that the most investigated parameters are the dimension of the FRP-plate, namely t_f and b_f (i.e., larger IQR); on the other hand, the dimension of the substrate, b_c, is generally the same in the experimental programs (i.e., IQR = 0.12) as well as the length (L_f) of the FRP bonded on the concrete block (i.e., IQR = 0.21). Finally, the mechanical proprieties of the FRP (E_f) and the concrete (f_c) results were explored; in fact, an IQR equal to 0.34 and 0.23 was reached for the compressive strength of the concrete and the elastic modulus of the FRP, respectively.
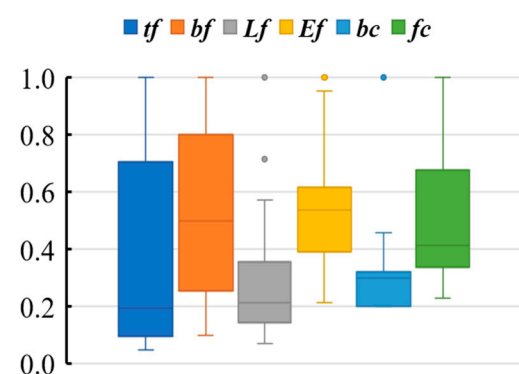
Figure 3. Variability ranges of the input-parameters by means the box plot representation.

Table 2. Interquartile ranges of the input parameters.

Parameter	t_f (mm)	b_f (mm)	L_f (mm)	E_f (GPa)	b_c (mm)	f_c (MPa)
Interquartile range (IQR)	0.61	0.55	0.21	0.23	0.12	0.34
Max	1.40	100	700	390	500	74
Min	0.083	10	50	83	100	17

5. ANN Proposed Model

The most significant parameters that were meaningful in the physical problem were considered as the inputs and a dimensionless output factor was selected, α, in order to define a reliable relationship furnishing the bond strength in terms of maximum debonding load, P_u. Therefore, the outcome analytical model may assume a simple formulation according to Equation (3). Moreover, known parameters are introduced, namely b_f, t_f and f_c; which are the width and the thickness of the FRP-plate and the concrete compressive strength, respectively. The main idea consists in computing the equivalent bond strength between the FRP and the concrete substrate by considering a reduction of the compressive strength of the concrete, i.e., $f_c \times \alpha^{-1}$. Therefore, the ultimate bond force can be easily calculated by multiplying the bond strength with the net-area of the FRP (=$b_f \times t_f$).

$$P_u = b_f \cdot t_f \cdot f_c \cdot \alpha^{-1} \tag{3}$$

The ANN-procedure can perform a theoretical formulation for the determination of α based on the specimen mechanical and geometrical characteristics. Thus, three dimensionless parameters were introduced in the neural-networks in order to find out the relationship, which links them to the outcome α. The mentioned inputs are expressed in Equations (4)–(6) and the distribution of their frequency, represented by the number of specimens, is illustrated by the histograms reported in Figure 4. Specifically, β has been included in order to consider the effect of the stress distribution in the area around the FRP-plate, which is mostly affected by the ratio between the dimension of the FRP itself and that of the substrate (see [23,65–67]). Moreover, the γ factor considers the influence of the bonded length, that affects the bond strength in relation to the effective bond length [18]. Finally, the mechanical property of the FRP has been considered in Equation (6), according to [65].

$$\beta = \frac{b_c}{b_f} \tag{4}$$

$$\gamma = \frac{L_f}{t_f} \tag{5}$$

$$\delta = \frac{E_f}{f_c} \tag{6}$$

The database includes 368 specimens, with the highest frequency of β between 1.2 and 3.3 with a minimum value of 1.0 and a maximum of 20.0 (Figure 4a). The α factor presents the most populated range from 74.1 to 441.7 Figure 4b. The δ factor is the most regularly distributed in the database with the top frequency of 120 specimens in the 2.3–3.9 range (Figure 4c). In computing δ the E_f is considered in GPa while fc is expressed in MPa.
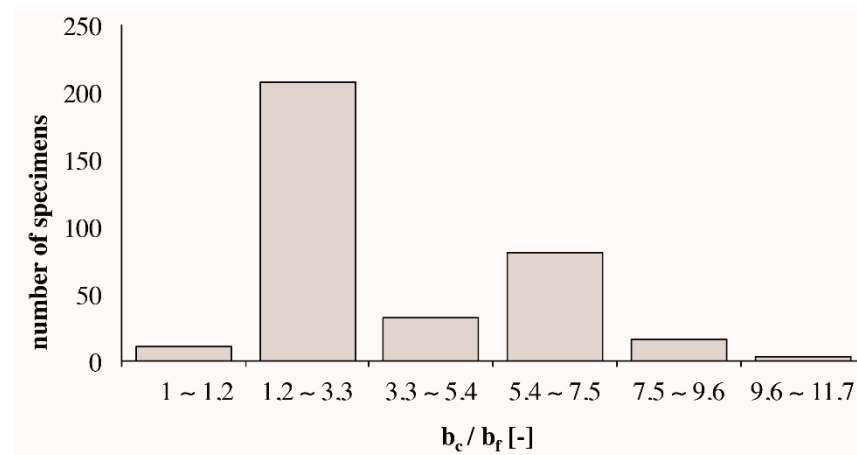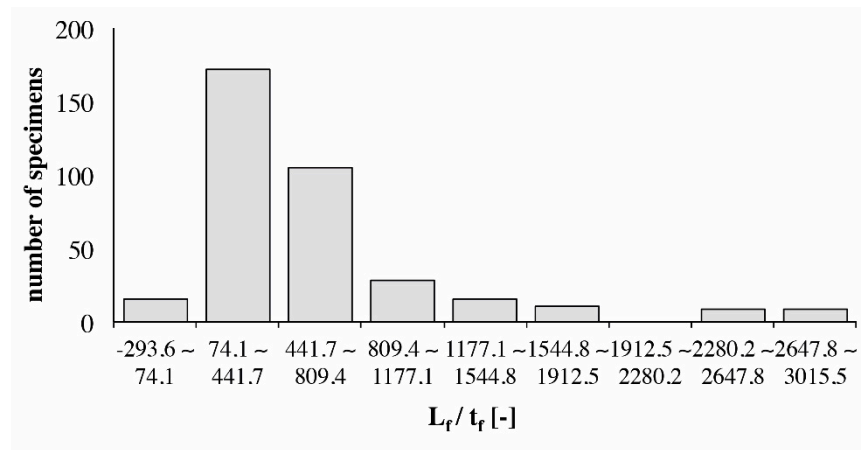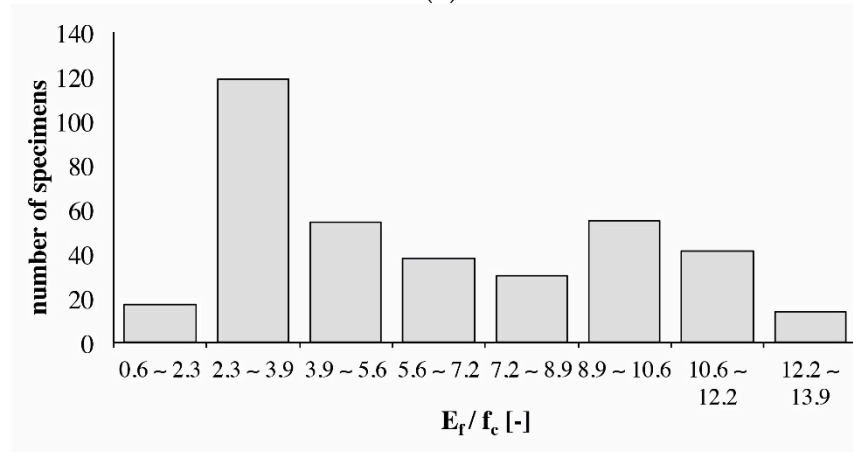
Figure 4. Distribution of data in terms of input parameters: (**a**) β, (**b**) γ and (**c**) δ.

A non-linear input-output model was implemented with a polynomial active neuron type in a 3-hidden-layers network. The generated model is listed from Equations (7)–(13). As evident, α was computed by a sequence of polynomial simple equations in which x variables are processed from the characteristics of the specimen expressed through β, γ and δ.

$$x_1 = -\frac{25.20}{10^5}\beta\gamma + 0.53 \tag{7}$$

$$x_2 = -0.24\delta + \frac{51.50}{10^4}\beta\gamma + 1.34 \tag{8}$$

$$x_3 = 0.81(x_1 + x_2) + 0.45x_1x_2 + 0.17x_1^2 \tag{9}$$

$$x_4 = -0.48\delta + \frac{18.74}{10^3}\delta^2 + 2.07 \tag{10}$$

$$x_5 = -\frac{42.07}{10^5}\gamma - 0.19\delta + 1.47 \tag{11}$$

$$x_6 = 1.13x_5 + 0.50x_5^2 - 0.39x_4^2 \tag{12}$$

$$\propto = 16.98x_6 + 28.21x_3 + 22.64x_6 + 38.99 \tag{13}$$

5.1. Model Evaluation

The theoretical value of the force P_u was then calculated by Equation (3). The frequency of the ratio between the experimental results and the predicted values is illustrated in Figure 5, where the normal distribution of the probability frequency (blue line) and the cumulative probability (red line) were both reported.
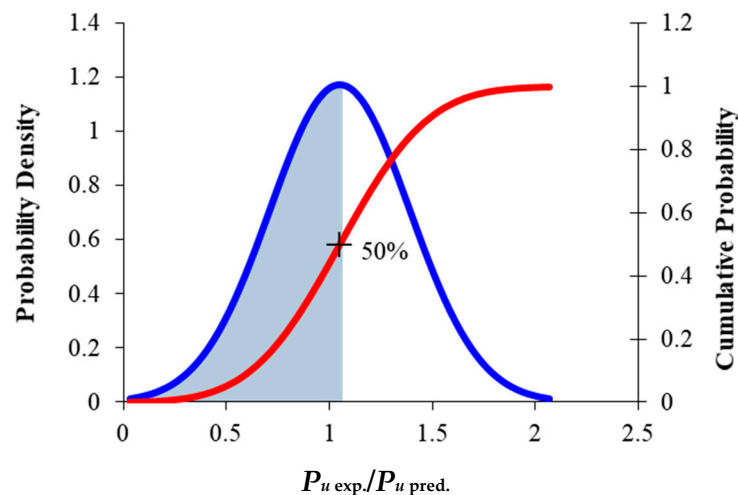
Figure 5. Distribution of the frequency of the experimental/predicted values of P_u.

The domain of the Gaussian function can be divided into quartiles in order to obtain the box plot graph reported in Figure 6 and Table 3. Four quartiles are identified (Q0, Q1, Q2 and Q3) and the median (Me) is represented by a marked line. The range Q1–Q3 represents the box in which the 50% of the statistical population is contained while the range Q0–Q4 includes the whole domain. The mutual size of these two ranges provides information about the accuracy of the model; in fact, the smaller is the box respect to the domain the greater is the accuracy of the predictions of the proposed model. On the other hand, the position of the box gives a measure of the precision; in fact, if the box is located close to 1.0 it means that the theoretical values are close to the experimental ones and if the Me is centered in the box and close to 1.0 it means that most of the predictions tend to coincide with the target value (experimental).

Table 3. Quartiles border values.

Quartile	Value
Q0	0.15
Q1	0.79
Q3	1.20
Q4	2.53
Me	1.01

The goodness of fit for the proposed model was performed firstly by verifying the linear correlation of the predicted results respect to the experimental ones in the quartile–quartile (Q–Q) range (Figure 7). Validation was run also by evaluating the prediction performance compared with the 368 tested specimens (Figure 8), found in literature. The robustness of the model was checked by analyzing the parametric influence of the considered input variables on the determination of the debonding ultimate force (Figures 9 and 10). The correlation factor (R^2) was calculated as equal to 0.95 in the box Q1–Q3 (see Figure 6 and Table 3) where more than 190 specimens are placed (Figure 7).
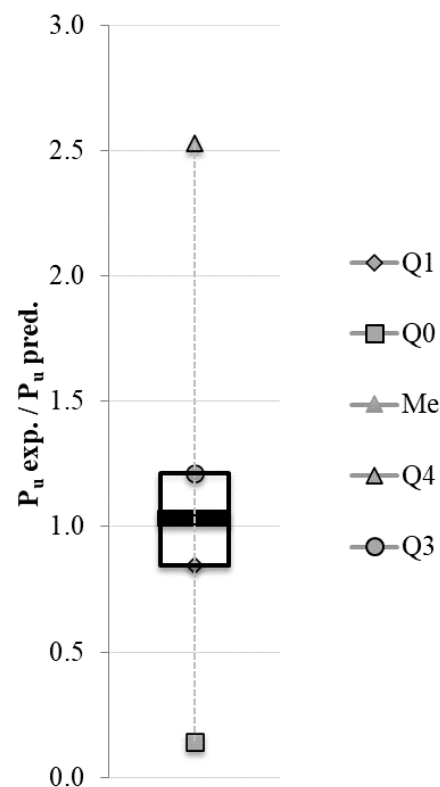
Figure 6. Box-plot of the frequency of the experimental/predicted values of P_u.
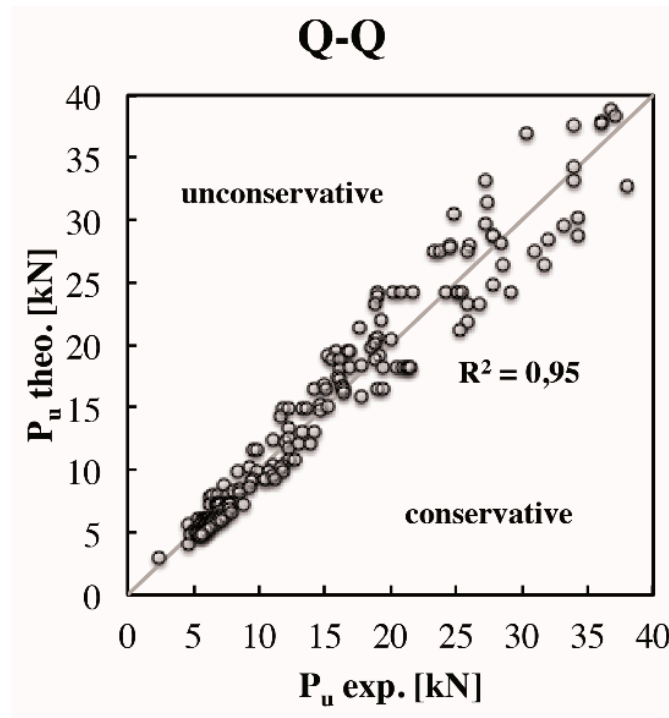
Figure 7. Experimental vs. theoretical correlation in the quartile–quartile range.

The grey area illustrated in Figure 8 is indicative of the validity of the model. A good match of the actual and predicted value of the P_u may be appreciated for the whole database. In particular, the specimens, with the worst forecast (i.e., larger scatter from the experimental relative result) are in the conservative side and represent the 15% of the whole population.
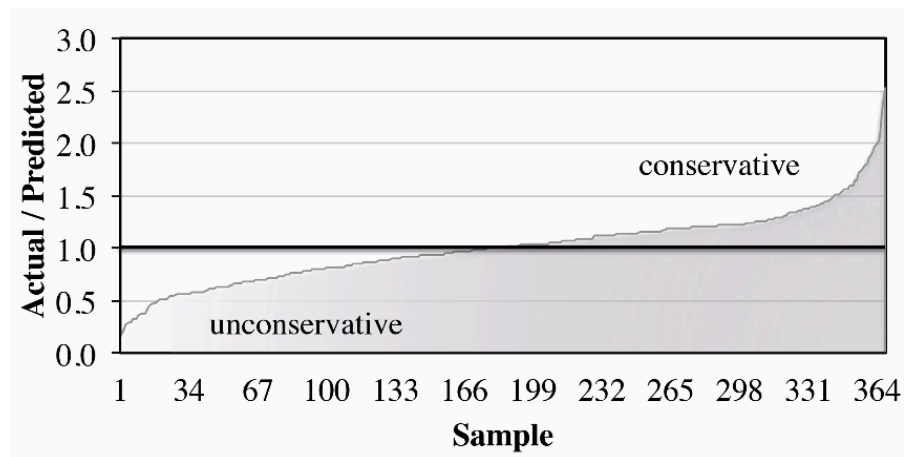
Figure 8. Area graph of the actual/predicted P_u.

5.2. Robustness Analysis

In Figures 9 and 10 the iso-parametric curves are reported, by varying two fundamental variables, such as the elastic modulus of the FRP and the width of the concrete substrate; in the first case the isoperimetric curves are plotted for different bond lengths, in the second diagram different concrete grades are assumed. As expected, for a fixed value of the elastic modulus of the FRP-plate, if the bond length increases also the debonding force increases (until the limit of the effective bond length). Considering a single iso-parametric curve, with a priori definition of the active bond length, the greater is the entity of the Young's modulus of the FRP-plate the greater is the force necessary to detach it from the concrete block. In fact, high quality of the fibers means minor elongation of the FRP sheet or

major force for inducing e unitary deformation according to [68]. Obviously, the theoretical model is assessed in order to catch the proportional relation between parameters, but the bond length must be limited by an upper bound equal to the effective bond length, experimentally determined (see [28–30,36,39]).
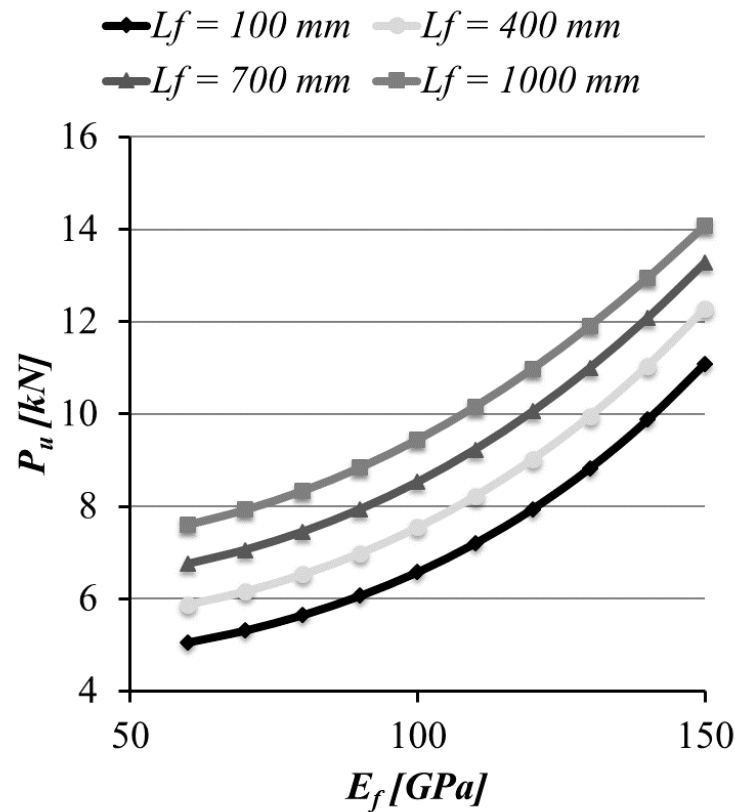
Figure 9. Influence of the Young's modulus of the FRP and the active bond length on the debonding force.

In Figure 10 the iso-parametric curves refer to constant values of the concrete compressive strength; the debonding load is plotted versus the width of the concrete block. The parametric study considers 20, 30, 40 and 50 MPa of the concrete compressive strength, which correspond to a value of the debonding force that increases up two times from 20 to 50 MPa of concrete resistance, at the same width. If the mechanical properties of the concrete increase, crack openings are delayed; therefore, the cohesive delamination within the concrete, that is the typical mode of failure occurs at higher load values. For example, concerning the 40 MPa compressive strength line, the increasing of the concrete width produces a small raise of the debonding force according to the experimental evidence (e.g., in [68]). Thus, the proposed model seems to be faithful to the trends that were found from the laboratory tests, as described in the literature database.
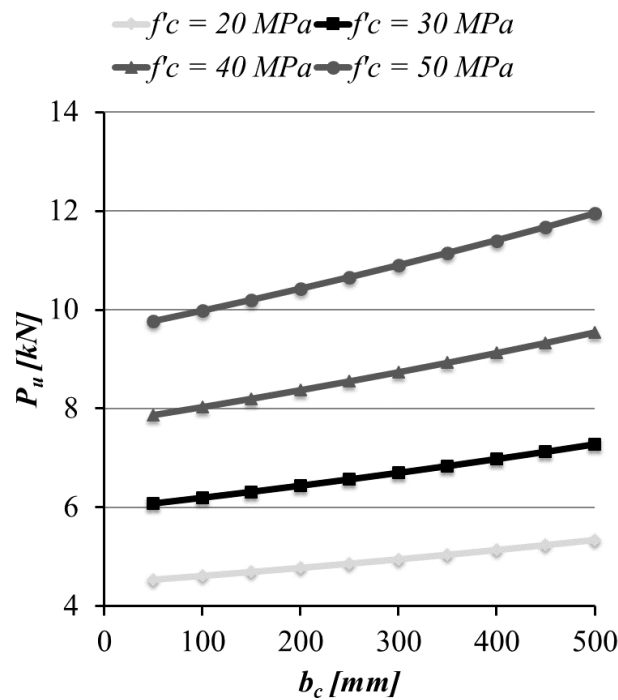
Figure 10. Influence of the width and the compressive strength of the concrete on the debonding force.

Since part of the concrete has been experienced to be pulled off in debonding tests, the tensile strength of the substrate plays a crucial role in the phenomena. For this reason, the sensitivity of the P_u prediction with respect to the f_c and f'_{ct} (compressive and tensile strength of the concrete respectively) input has been investigated according to Figure 11. A proportional pseudo linear correlation was found, with a gradient that slightly increases for high levels of concrete compressive strength (45–60 MPa) according to the tensile strength (2.5–3.0 MPa). Whereby, the analytical results are reliable with experimentations.
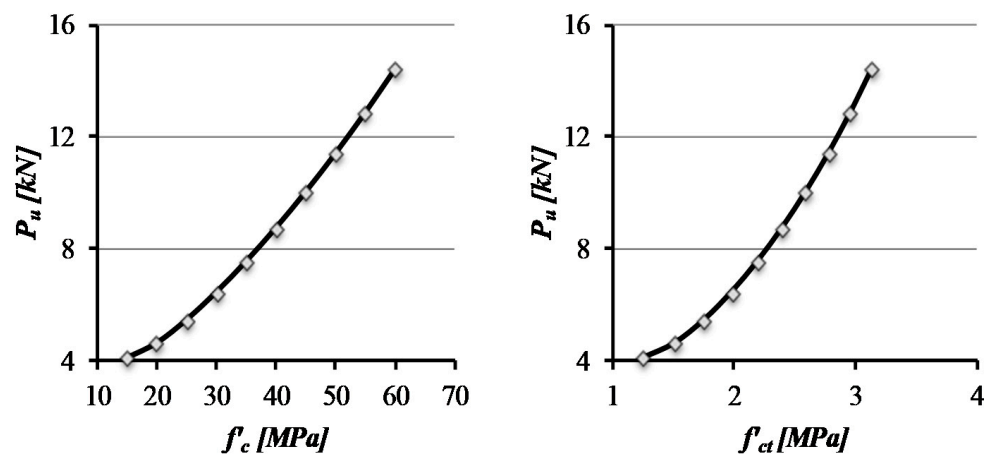
Figure 11. Influence of the concrete compressive (**left**) and tensile (**right**) strength on the debonding force.

Further important consideration can be carried out from the calculation of the percentage increment of mean square error (%IncMSE). It refers to the mean increase of the accuracy of the theoretical model. The higher the %IncMSE is, the more important the parameter is that is involved in the global prediction of the target. It allows in finding the contribution a particular variable makes to the prediction of a criterion variable (target) in combination with other predictor variables according to Equation (14). The comparison of the %IncMSE for the imposed inputs is reported in Figure 12. It can be observed that δ is the input which more affect the accurate prediction of the outcome, while β and γ achieved comparable importance in the model performance. In other words, the bond strength is mostly affected by the mechanical properties of the FRP and the substrate. Contrarily, the substrate block dimensions less influenced the result, according to [68].

$$\%\text{IncMSE} = \frac{\sum SE}{A \cdot n} \cdot 100 \tag{14}$$

where:

- SE is the square error between the experimental and theoretical values;
- A is the SE higher response integer;
- n total number of respondents.
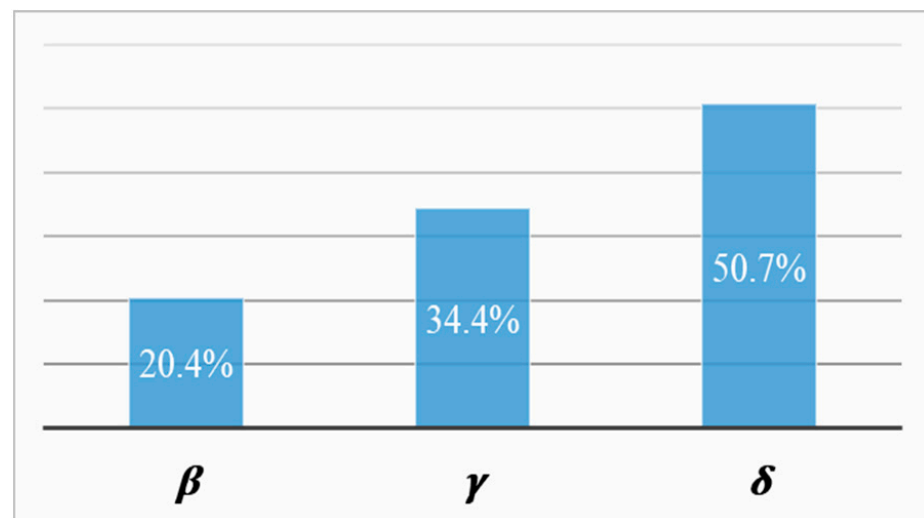
Figure 12. Variable of importance: the %IncMSE.

6. Comparison with Existing Analytical Models

A comparison between the theoretical values of the bond strength at the interface between FRP and concrete, predicted by the existing models, is presented in this section. A statistical representation of the capacity of the models to catch accurately the experimental values is illustrated in Figure 13 and Table 4. In Figure 13 the results of the proposed model are highlighted in the grey area. The ability of the model depends on the accuracy and the precision in correlating through a linear relationship the experimental results with those theoretically computed. In this scenario, the box plot representation of Figure 13 seems the best tool to for the mentioned goal. Moreover, Table 4 provides numerical outcomes, further supporting the analysis of the comparison.

It should be remarked that Figure 13 and Table 4 are organized by reporting the increasing of the interquartile range (IQR), in order to obtain an immediate graphic evaluation of the models, as the smaller the IQR is, the more accurate the predictions are. The box-plot presents models with an increasing accuracy by starting from the left to the right in Figure 12 and from top to down in Table 5. Another key-issue is represented by the position of the box, which should be centered in when a precise prediction is found. For example, the models reported in [30,34] are characterized by the smallest dimension of the box, but distant from the unity, thus it can be considered an accurate, but not the precise proposal. Moreover, the position of the Me inside of the box indicates the type of predictions distribution in the Q–Q, namely symmetrical or not symmetrical. In fact, if Me is centered in the box, predictions are symmetrically disposed; it does not happen, for example, in the Chen and Teng model [30]. The kurtosis of the Gaussian curve is also calculated in Equation (15).

$$K = \frac{\sum_{i=1}^{n} \left(\frac{x_i - \mu}{\sigma}\right)^4}{n} = 3.12 \tag{15}$$

The following situations may occur by concerning about the kurtosis coefficient, K:

- $K > 0$: the curve is defined leptokurtic, i.e., more "pointed" of a normal;
- $K < 0$: the curve is defined platykurtic, that is "flatter" than a normal;
- $K = 0$ the curve is defined normocurtica, i.e., "flat" as a normal.

Commonly, a value of the kurtosis of 3 is accepted as sufficient level for considering the frequency distribution as normal (see [69]). The precision of the frequency curve can be evaluated with the asymmetry of the mode (as1) and with the first and the second asymmetry Pearson's coefficients (as2 and as3) expressed in Equations (16)–(18) respectively.

$$as1 = \frac{\mu - Mo}{\sigma} \tag{16}$$

$$as2 = \frac{3(\mu - Mo)}{\sigma} \tag{17}$$

$$as3 = \frac{3(\mu - Me)}{\sigma} \tag{18}$$

where:

- Mo is the mode.
- μ is the average value.
- σ is the standard deviator.

Thus, the position of the box plot provides information about the accuracy of the model: if the entire box plot is far from 1 it implies that experimental values are non-linearly related to the theoretical outcomes. On the other hand, the position of the box with respect to the Me specifies if the model is precise or not as well as the Pearson's coefficients (as1, as2 and as3); the Kurtosis (K) gives a measure of the accuracy, i.e., the lower are the Pearson's coefficients and the more precise is the prediction and contemporary the higher is the kurtosis the more is the accuracy of the prediction (see [46]). In Table 5, the best value of IQR (min), K (max) and as1, as2 and as3 (min) are reported in bold. The proposed model exhibits the maximum value of K and the minimum of as1, as2 and as3. Based on the present study, the less accurate predictions were provided by very dated proposals (i.e., [24–27]) that do not evidence the importance enough of the mechanical parameter of the FRP, disagreeing with Figure 12.
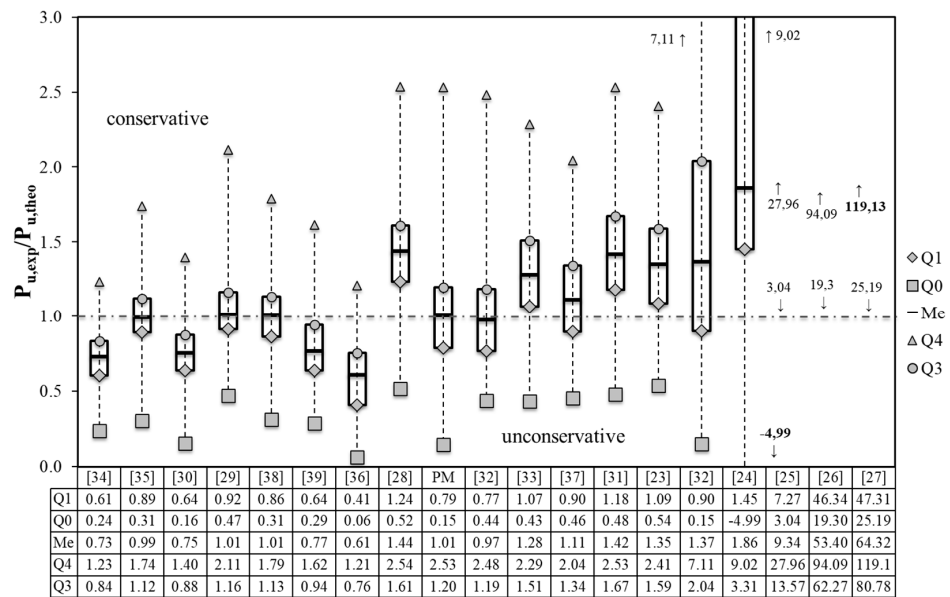
Figure 13. Variable of importance: the %IncMSE.

Table 4. Comparison of the precision and the accuracy of the analyzed models.

References	Year	IQR	K	as1	as2	as3
[34]	2005	0.23	2.88	0.00	0.00	−0.11
[35]	2005	0.23	3.75	0.00	0.00	0.25
[30]	2001	0.24	3.28	0.00	0.00	0.09
[29]	2001	0.25	4.49	0.50	1.50	0.50
[38]	2012	0.27	3.24	0.50	1.50	0.08
[39]	2013	0.30	3.09	0.00	0.00	0.34
[36]	2009	0.35	2.45	−0.50	−1.50	−0.25
[28]	2000	0.38	3.17	0.50	1.50	0.11
Proposed Model [–]	-	0.41	4.86	0.00	0.00	0.00
[32]	2003	0.42	4.69	−0.50	−1.50	0.11
[33]	2004	0.44	2.64	0.00	0.00	0.01
[37]	2010	0.45	4.02	0.00	0.00	0.72
[31]	2001	0.45	2.70	0.50	1.50	0.24
[23]	1994	0.49	2.64	0.00	0.00	0.01
[22]	1980	1.14	7.76	0.50	1.50	0.52
[24]	1996	1.85	7.43	0.50	1.50	1.02
[25]	1997	6.29	3.55	0.50	1.50	0.90
[26]	1997	15.92	3.16	0.00	0.00	0.36
[27]	1998	33.46	2.17	−0.50	−1.50	0.09
Max		33.46	7.76	0.50	1.50	1.02
Min		0.23	2.17	0.00	0.00	0.00

A further consideration about the validity of the proposed model can be done based on statistical parameters such as the RRMSE (relative root mean square error), the MAE (mean absolute error) and the MAPE (mean absolute percentage error), expressed by Equations (19)–(21) respectively. Specifically, the RRMSD represents the standard deviation of the differences between the predicted values and the observed values (i.e., the calculation of the residuals) while the MAE and the MAPE are a measure of the average distance between two or more observations and the respective predictions in terms of dimension and dimensionless parameter, respectively. In other words, the MAE (or the MAPE) uses the same scale as the data being measured while the RRMSE reflects a kind of weight factor

related to the square of the computed error. All the models were used with the same data base for calculation of the RRMSE, MAE, MAPE, and R^2.

$$\text{RRMSE} = \frac{1}{n}\sqrt{\sum_{i=1}^{n}\left(\frac{y_i - \hat{y}_i}{y_i}\right)^2} \cdot 100 \tag{19}$$

$$\text{MAE} = \frac{1}{n}\sum_{i=1}^{n}\left|y_i - \hat{y}_i\right| \tag{20}$$

$$\text{MAPE} = \frac{1}{n}\sum_{i=1}^{n}\left|\frac{y_i - \hat{y}_i}{y_i}\right| \cdot 100 \tag{21}$$

This section is not mandatory but may be added if there are patents resulting from the work reported in this manuscript.

where:

- n is the number of samples in the input database,
- i is the general sample,
- y_i is the experimental value,

 $\hat{y}_i$ is the theoretical value.

The minimum values of the RRMSE, MAE and MAPE correspond to the minimum scatter and the best ability of the theoretical procedure to predict the experimental results. The analytical models cited in the background section are consequently compared in Figure 14 and Table 5 respectively from a graphical and numerical point of view. Moreover, a comparison also including the correlation coefficient R^2 is reported in Figure 15. A deep evaluation and comparison of the literature analytical models and of the proposed one can be carried out. In fact, the predictive performance can be evaluated in terms of the best agreement of precision, accuracy and linear correlation between the experimental and theoretical values (see [46]). From this perspective, the precise model corresponds to the nearness of the average, the median and the mode (to each other) of the frequency of the ratio between the experimental and the theoretical outcomes. The accuracy is measured by the proximity of the average, the median and the mode to 1 and, at the same time, the lower value of the MAPE. The correlation is commonly computed by the R^2 factor (the more R^2 is close to 1 the higher is the correlation between variables). According to Figure 15, the models [24–27] give the worst predictions of the ultimate bond force; the reason could be related to the low weight attributed to the elastic modulus of the reinforcement, which resulted to affect mostly the accurate prediction of the target (see Figure 12). Controversially, the proposed model and the proposal reported in [35] have demonstrated to provide the best predictions of the failure of the FRP-to-concrete in pull-pull shear test.

Except for the proposed model, there are few other models demonstrating good predictive capacity, such as [28,31,53].

Table 5. Statistical coefficients determination for the considered models.

References	RRMSE (%)	MAE (kN)	MAPE (%)	R^2
[34]	2.00%	3.34	20.00%	0.98
[35]	0.00%	0.46	0.60%	0.99
[30]	1.00%	2.87	17.00%	0.97
[29]	0.00%	0.46	1.10%	0.99
[38]	0.00%	0.61	0.40%	0.98
[39]	1.00%	2.71	15.00%	0.96
[36]	3.00%	6.35	37.00%	0.90
[28]	1.00%	2.26	15.00%	0.98
Proposed Model [–]	0.00%	0.84	0.30%	0.95

Table 5. *Cont.*

References	RRMSE (%)	MAE (kN)	MAPE (%)	R^2
[32]	1.00%	1.09	1.80%	0.95
[33]	1.00%	1.67	10.00%	0.97
[37]	0.00%	0.95	1.10%	0.94
[31]	1.00%	0.96	4.90%	0.95
[23]	1.00%	2.29	14.00%	0.97
[22]	1.00%	2.27	12.00%	0.86
[24]	2.00%	4.05	24.70%	0.80
[25]	3.00%	7.69	44.70%	0.93
[26]	4.00%	8.43	49.10%	0.98
[27]	4.00%	7.56	48.90%	0.90
Max	4.00%	8.43	49.10	0.99
Min	0.00	0.46	0.30%	0.80

Nowadays, FRPs suffer the competition of FRCM (fabric reinforced cementitious matrix) due to the higher compatibility of the inorganic matrix with existing substrates ([70,71]). The proposed formulation is assumed to be not valid in case of FRCM because the properties of the matrix were neglected in the ANN-calibration [72–74].
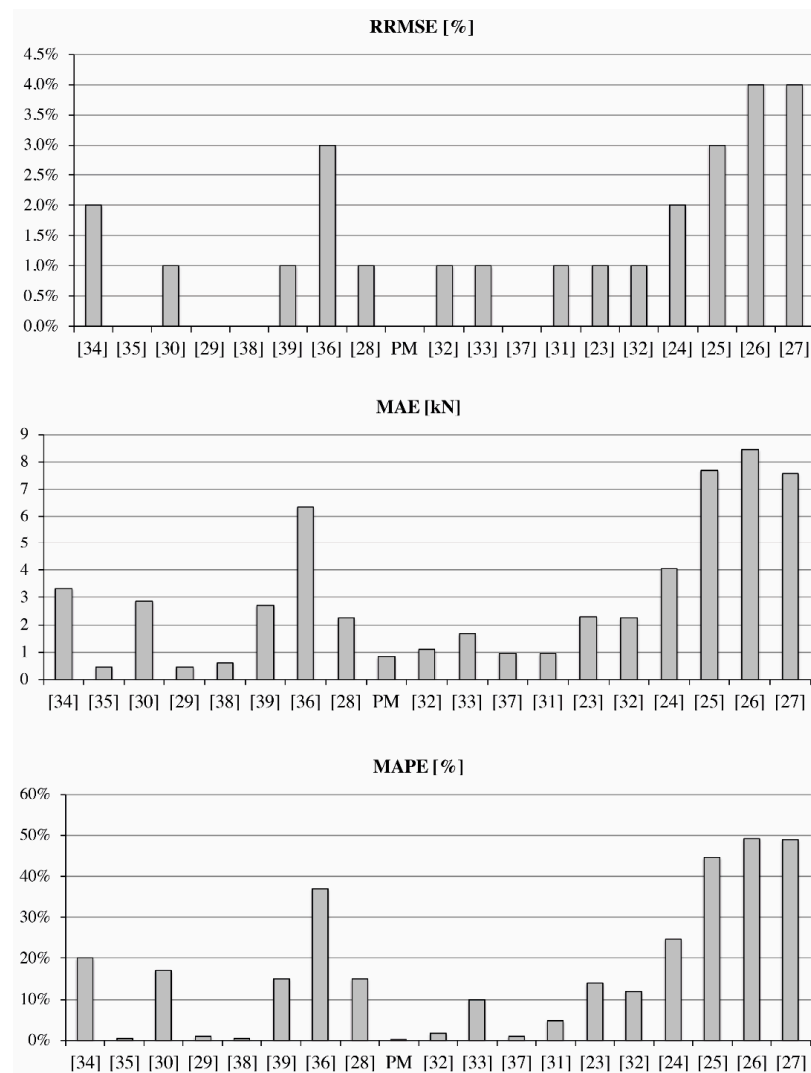
Figure 14. Statistical coefficients: RRMSE (**top**), MAE (**middle**) and MAPE (**bottom**).

	[34]	[35]	[30]	[29]	[38]	[39]	[36]	[28]	PM	[32]	[33]	[37]	[31]	[23]	[32]	[24]	[25]	[26]	[27]
Average	0.73	1.01	1.10	0.76	1.36	0.79	1.01	1.05	1.01	1.14	1.53	10.87	0.99	1.42	0.59	2.43	10.87	54.98	64.95
Median	0.73	0.99	1.02	0.75	1.35	0.77	1.01	1.01	1.01	1.11	1.37	9.34	0.97	1.42	0.61	1.86	9.34	53.40	64.32
Mode	0.73	1.01	1.10	0.76	1.52	0.79	0.90	0.94	1.01	0.98	1.07	8.30	1.13	1.42	0.71	1.59	8.30	54.98	75.45
MAPE [%]	0.2	0.006	0.17	0.011	0.004	0.15	0.37	0.15	0.003	0.018	0.1	0.011	0.049	0.14	0.12	0.247	0.447	0.491	0.489
R2	0.98	0.99	0.97	0.99	0.98	0.96	0.9	0.98	0.95	0.95	0.97	0.94	0.95	0.97	0.86	0.8	0.93	0.98	0.9

Figure 15. Comparison of the performance of the analytical models with respect the proposed one.

7. Conclusions

A new empirical model for the prediction of the ultimate bond retention load between an FRP plate/strip and a concrete rigid substrate was presented and discussed within the paper. It is based on an artificial neural networks (ANN) approach that was applied to a large database including 368 available experimental results available from scientific literature. The proposed formulation was found to be effective both in terms of accuracy and precision, thus it can be considered competitive with the available existing analytical models reported in the present study. A parametric study was used to test the robustness of the proposed model. The results confirmed that the presented equation is consistent with the debonding phenomena observed for an FRP plate glued to a concrete block, when subjected to a single lap shear test. A good correlation of the actual and predicted values is shown as well as the outcome of the selected database of 368 specimens. The predictions were found acceptable for almost 65% of the population and conservative in the cases of inaccurate predictions. This result can be considered significant, due to the very brittle nature of the studied mechanical phenomena. The ANN method seems to be a powerful tool, which can be used in order to detect patterns in a large database, made by inhomogeneous data, and extract knowledge from it. The proposed model shows the advantages to be a simple formulation composed of a sequence of polynomial equations and a continuous function, which is formally different from the most available models, that considers varying functions to depend mainly on the active bond length.

Potential development of the proposed model is implementing factors in order to consider further variables affecting the bond strength, such as the type of the laminate, surface treatment, adhesive type, thickness, etc.

Appendix A

Table A1. Database of FRP-plate vs. concrete substrate bond test.

References	Specimen Label	t_f (mm)	b_f (mm)	L_f (mm)	E_f (GPa)	b_c (mm)	f_c (MPa)	P_u (kN)
[47]	C1	1.016	25.4	76.2	108.478	228.6	36.1	8.462
	C2	1.016	25.4	76.2	108.478	228.6	47.1	9.931
	C3	1.016	25.4	76.2	108.478	228.6	47.1	10.683
	C4	1.016	25.4	76.2	108.478	228.6	47.1	10.683
	C5	1.016	25.4	76.2	108.478	228.6	43.6	10.531
	C7	1.016	25.4	76.2	108.478	228.6	43.6	9.61
	C8	1.016	25.4	76.2	108.478	228.6	43.6	10.518
	C9	1.016	25.4	76.2	108.478	228.6	43.6	11.199
	C10	1.016	25.4	76.2	108.478	228.6	24	9.869
	C11	1.016	25.4	76.2	108.478	228.6	28.9	9.343
	C12	1.016	25.4	76.2	108.478	228.6	43.7	11.204
	C13	1.016	25.4	76.2	108.478	228.6	36.4	8.094
	C14	1.016	25.4	76.2	108.478	228.6	36.4	12.811
	C15	1.016	25.4	76.2	108.478	228.6	36.4	11.917
	C16	1.016	25.4	76.2	108.478	228.6	36.4	11.57
[48]	1_11	0.167	40	100	230	100	28.88	8.75
	1_12	0.167	40	100	230	100	26.66	8.85
	1_21	0.167	40	200	230	100	28.88	9.3
	1_22	0.167	40	200	230	100	26.66	8.5
	1_31	0.167	40	300	230	100	28.88	9.3
	1_32	0.167	40	300	230	100	26.66	8.3
	1_41	0.167	40	500	230	100	28.88	8.05
	1_42	0.167	40	500	230	100	28.88	8.05
	1_51	0.167	40	500	230	100	26.47	8.45
	1_52	0.167	40	500	230	100	26.47	7.3
	2_11	0.167	40	100	230	100	24.99	8.75
	2_12	0.167	40	100	230	100	24.99	8.85
	2_13	0.167	40	100	230	100	26.17	7.75
	2_14	0.167	40	100	230	100	26.17	7.65
	2_15	0.167	40	100	230	100	24.4	9
	2_21	0.167	40	100	230	100	24.99	12
	2_22	0.167	40	100	230	100	24.99	10.8
	2_31	0.167	40	100	230	100	24.99	12.65
	2_32	0.167	40	100	230	100	24.99	14.35
	2_41	0.167	40	100	230	100	24.4	11.55
	2_42	0.167	40	100	230	100	24.4	11
	2_51	0.167	40	100	230	100	26.17	9.85
	2_52	0.167	40	100	230	100	26.17	9.5
	2_61	0.167	40	100	230	100	26.17	8.8
	2_62	0.167	40	100	230	100	26.17	9.25
	2_71	0.167	40	100	230	100	26.17	7.65
	2_71	0.167	40	100	230	100	26.17	6.8
	2_81	0.167	40	100	230	100	49.97	7.75
	2_82	0.167	40	100	230	100	49.97	8.05
	2_91	0.167	40	100	230	100	24.4	6.75
	2_92	0.167	40	100	230	100	24.4	6.8
	2_101	0.167	40	100	230	100	24.99	7.7
	2_102	0.167	40	100	230	100	26.17	6.95

Table A1. *Cont.*

References	Specimen Label	t_f (mm)	b_f (mm)	L_f (mm)	E_f (GPa)	b_c (mm)	f_c (MPa)	P_u (kN)
	I-1	0.165	25	75	256	150	23	4.75
	I-2	0.165	25	85	256	150	23	5.69
	I-3	0.165	25	95	256	150	23	5.76
	I-4	0.165	25	95	256	150	23	5.76
	I-5	0.165	25	95	256	150	23	6.17
	I-6	0.165	25	115	256	150	23	5.96
	I-7	0.165	25	145	256	150	23	5.95
	I-8	0.165	25	190	256	150	23	6.68
	I-9	0.165	25	190	256	150	23	6.35
	I-10	0.165	25	95	256	150	23	6.17
	I-11	0.165	25	75	256	150	23	5.72
	I-12	0.165	25	85	256	150	23	6
	I-13	0.165	25	95	256	150	23	6.14
	I-14	0.165	25	115	256	150	23	6.1
	I-15	0.165	25	145	256	150	23	6.27
	I-16	0.165	25	190	256	150	23	7.03
	II-1	0.165	25	95	256	150	22.9	5.2
	II-2	0.165	25	95	256	150	22.9	6.75
	II-3	0.165	25	95	256	150	22.9	5.51
	II-4	0.165	25	190	256	150	22.9	7.02
	II-5	0.165	25	190	256	150	22.9	7.07
	II-6	0.165	25	190	256	150	22.9	6.98
	III-1	0.165	25	100	256	150	27.1	5.94
	III-2	0.165	50	100	256	150	27.1	11.66
	III-3	0.165	75	100	256	150	27.1	14.63
	III-4	0.165	100	100	256	150	27.1	19.07
	III-7	1.27	25	100	225	150	27.1	4.78
	IV-1	0.165	25	95	256	150	18.9	5.86
	IV-2	0.165	25	95	256	150	18.9	5.9
	IV-3	0.165	25	95	256	150	19.8	5.43
	IV-4	0.165	25	95	256	150	19.8	5.76
[49]	IV-5	0.165	25	95	256	150	18.9	5
	IV-6	0.165	25	95	256	150	19.8	7.08
	IV-7	0.165	25	95	256	150	18.9	5.5
	IV-8	0.165	25	95	256	150	19.8	5.93
	IV-9	0.165	25	95	256	150	18.9	5.38
	IV-10	0.165	25	95	256	150	19.8	6.6
	IV-11	0.165	25	95	256	150	18.9	5.51
	IV-12	0.165	25	95	256	150	19.8	5.67
	IV-13	0.165	25	95	256	150	18.9	6.31
	IV-14	0.165	25	95	256	150	19.8	6.19
	V-1	0.165	15	95	256	150	21.1	3.81
	V-2	0.165	15	95	256	150	21.1	4.41
	V-3	0.165	25	95	256	150	21.1	6.26
	V-4	0.165	50	95	256	150	21.1	12.22
	V-5	0.165	75	95	256	150	21.1	14.29
	V-6	0.165	100	95	256	150	21.1	15.58
	VI-1	0.165	25	95	256	150	21.9	6.01
	VI-2	0.165	25	95	256	150	21.9	5.85
	VI-3	0.165	25	145	256	150	21.9	5.76
	VI-4	0.165	25	145	256	150	21.9	5.73
	VI-5	0.165	25	190	256	150	21.9	5.56

Table A1. *Cont.*

References	Specimen Label	t_f (mm)	b_f (mm)	L_f (mm)	E_f (GPa)	b_c (mm)	f_c (MPa)	P_u (kN)
	VI-6	0.165	25	190	256	150	21.9	5.58
	VI-7	0.165	25	240	256	150	21.9	5.91
	VI-8	0.165	25	240	256	150	21.9	5.05
	VII-1	0.165	25	95	256	150	24.9	6.8
	VII-2	0.165	25	95	256	150	24.9	6.62
	VII-3	0.165	25	145	256	150	24.9	7.33
	VII-4	0.165	25	145	256	150	24.9	6.49
	VII-5	0.165	25	190	256	150	24.9	7.07
	VII-6	0.165	25	190	256	150	24.9	7.44
	VII-7	0.165	25	240	256	150	24.9	7.16
	VII-8	0.165	25	240	256	150	24.9	6.24
	I-3	0.825	50	100	110	200	17	11.64
	I-4	0.99	50	100	110	200	17	12.86
	II-1	0.495	50	100	110	200	46.2	12.55
	II-2	0.66	50	100	110	200	46.2	14.25
[50]	II-3	0.825	50	100	110	200	46.2	17.72
	II-4	0.99	50	100	110	200	46.2	18.86
	III-1	0.495	50	100	110	200	61.5	13.24
	III-2	0.66	50	100	110	200	61.5	15.17
	III-3	0.825	50	100	110	200	61.5	18.86
	III-4	0.99	50	100	110	200	61.5	19.03
	PG1-11	0.169	50	130	97	100	37.6	7.78
	PG1-12	0.169	50	130	97	100	37.6	9.19
	PG1-1W1	0.169	75	130	97	100	37.6	10.11
	PG1-1W2	0.169	75	130	97	100	37.6	13.95
	PG1-1L11	0.169	50	100	97	100	37.6	6.87
[51]	PG1-1L12	0.169	50	100	97	100	37.6	9.2
	PG1-1L21	0.169	50	70	97	100	37.6	6.46
	PG1-1L22	0.169	50	70	97	100	37.6	6.66
	PG1-21	0.338	50	130	97	100	37.6	10.49
	PG1-22	0.338	50	130	97	100	37.6	11.43
	PC1-1C1	0.111	50	130	235	100	37.6	9.97
	PC1-1C2	0.111	50	130	235	100	37.6	9.19
	NJ2	0.083	100	100	240	150	20.5	11
	NJ3	0.083	100	150	240	150	20.5	11.25
	NJ4	0.083	100	100	240	150	36.7	12.5
	NJ5	0.083	100	150	240	150	36.7	12.25
	NJ6	0.083	100	150	240	150	36.7	12.75
	DLUT5-2G	0.507	20	150	83.03	150	28.7	5.81
	DLUT5-5G	0.507	50	150	83.03	150	28.7	10.6
	DLUT5-7G	0.507	80	150	83.03	150	28.7	18.23
	DLUT30-1G	0.507	20	100	83.03	150	45.3	4.63
	DLUT30-2G	0.507	20	150	83.03	150	45.3	5.77
	DLUT30-3G	0.507	50	60	83.03	150	45.3	9.42
[52,53]	DLUT30-4G	0.507	50	100	83.03	150	45.3	11.03
	DLUT30-6G	0.507	50	150	83.03	150	45.3	11.8
	DLUT30-7G	0.507	80	100	83.03	150	45.3	14.65
	DLUT30-8G	0.507	80	150	83.03	150	45.3	16.44
	DLUT50-1G	0.507	20	100	83.03	150	55.5	5.99
	DLUT50-2G	0.507	20	150	83.03	150	55.5	5.9
	DLUT50-4G	0.507	50	100	83.03	150	55.5	9.84
	DLUT50-5G	0.507	50	150	83.03	150	55.5	12.28

Table A1. *Cont.*

References	Specimen Label	t_f (mm)	b_f (mm)	L_f (mm)	E_f (GPa)	b_c (mm)	f_c (MPa)	P_u (kN)
	DLUT50-6G	0.507	80	100	83.03	150	55.5	14.02
	DLUT50-7G	0.507	80	150	83.03	150	55.5	16.71
	DLUT15-2C	0.33	20	150	207	150	28.7	5.48
	DLUT15-5C	0.33	50	150	207	150	28.7	10.02
	DLUT15-7C	0.33	80	150	207	150	28.7	19.27
	DLUT30-1C	0.33	20	100	207	150	45.3	5.54
	DLUT30-2C	0.33	20	150	207	150	45.3	4.61
	DLUT30-4C	0.33	50	100	207	150	45.3	11.08
	DLUT30-5C	0.33	50	100	207	150	45.3	16.1
	DLUT30-6C	0.33	50	150	207	150	45.3	21.71
	DLUT30-7C	0.33	80	100	207	150	45.3	22.64
	DLUT50-1C	0.33	20	100	207	150	55.5	5.78
	DLUT50-4C	0.33	50	100	207	150	55.5	12.95
	DLUT50-5C	0.33	50	150	207	150	55.5	16.72
	DLUT50-6C	0.33	80	100	207	150	55.5	16.24
	DLUT50-7C	0.33	80	150	207	150	55.5	22.8
	Ueda_A1	0.11	50	75	230	100	29.74	6.25
	Ueda_A2	0.11	50	150	230	100	52.31	9.2
	Ueda_A3	0.11	50	300	230	100	52.31	11.95
	Ueda_A4	0.22	50	75	230	100	55.51	10
	Ueda_A5	0.11	50	150	230	100	54.36	7.3
	Ueda_A6	0.165	50	65	372	100	54.36	9.55
	Ueda_A7	0.22	50	150	230	100	54.75	16.25
	Ueda_A8	0.11	50	700	230	100	54.75	11
[54]	Ueda_A9	0.11	50	150	230	100	51.03	10
	Ueda_A10	0.11	10	150	230	100	30.51	2.4
	Ueda_A11	0.11	20	150	230	100	30.51	5.35
	Ueda_A12	0.33	20	150	230	100	30.51	9.25
	Ueda_A13	0.55	20	150	230	100	31.67	11.75
	Ueda_B1	0.11	100	200	230	500	31.67	20.6
	Ueda_B2	0.33	100	200	230	500	52.44	38
	Ueda_B3	0.33	100	200	230	500	58.85	34
	D-CFS-150-30 a	0.083	100	300	230	100	58.85	12.2
	D-CFS-150-30 b	0.083	100	300	230	100	73.85	11.8
	D-CFS-150-30 c	0.083	100	300	230	100	73.85	12.25
	D-CFS-300-30 a	0.167	100	300	230	100	73.85	18.9
	D-CFS-300-30 b	0.167	100	300	230	100	73.85	16.95
	D-CFS-300-30 c	0.167	100	300	230	100	73.85	16.65
	D-CFS-600-30 a	0.333	100	300	230	100	73.85	25.65
	D-CFS-600-30 b	0.333	100	300	230	100	73.85	25.35
	D-CFS-600-30 c	0.333	100	300	230	100	73.85	27.25
[55]	D-CFM-300-30 a	0.167	100	300	390	100	73.85	19.5
	D-CFM-300-30 b	0.167	100	300	390	100	73.85	19.5
	S-CFS-400-25 a	0.222	40	250	230	100	73.85	15.4
	S-CFS-400-25 b	0.222	40	250	230	100	73.85	13.9
	S-CFS-400-25 c	0.222	40	250	230	100	73.85	13
	S-CFM-300-25 a	0.167	40	250	390	100	73.85	12
	S-CFM-300-25 b	0.167	40	250	390	100	73.85	11.9
	S-CFM-900-25 a	0.5	40	250	390	100	73.85	25.9
	S-CFM-900-25 b	0.5	40	250	390	100	73.85	23.4
	S-CFM-900-25 c	0.5	40	250	390	100	73.85	23.7

Table A1. *Cont.*

References	Specimen Label	t_f (mm)	b_f (mm)	L_f (mm)	E_f (GPa)	b_c (mm)	f_c (MPa)	P_u (kN)
	C165-100	1.2	50	100	165	100	29.7	18.25
	C165-130	1.2	50	130	165	100	29.7	24.5
	C165-150	1.2	50	150	165	100	29.7	28.44
	C165-175	1.2	50	175	165	100	29.7	32
	C165-200	1.2	50	200	165	100	29.7	34.22
	C165-250	1.2	50	250	165	100	29.7	33.14
	C165-300	1.2	50	300	165	100	29.7	34.24
	CFRP-C210	1.2	50	150	210	100	35.8	30.4
[56]	C210-180	1.2	50	180	210	100	35.8	34
	C210-190	1.2	50	190	210	100	35.8	36
	C210-200	1.2	50	200	210	100	35.8	36.02
	C210-230	1.2	50	230	210	100	35.8	37.02
	C210-255	1.2	50	255	210	100	35.8	36.8
	CFRP-C300	1.2	50	160	300	100	29.7	38.02
	C300-180	1.2	50	180	300	100	29.7	41.15
	C300-200	1.2	50	200	300	100	29.7	46.35
	C300-250	1.2	50	250	300	100	29.7	45.5
	C300-300	1.2	50	300	300	100	29.7	45.95
	-	1.4	10	50	152.2	200	30	5.15
	-	1.4	10	100	152.2	200	30	7.55
	-	1.4	10	150	152.2	200	30	7.7
	-	1.4	10	200	152.2	200	30	7.9
	-	1.4	10	250	152.2	200	30	6.25
	-	1.4	10	300	152.2	200	30	7.58
	-	1.4	10	50	152.2	200	40	5.1
	-	1.4	10	100	152.2	200	40	6.85
	-	1.4	10	150	152.2	200	40	6.35
	-	1.4	10	200	152.2	200	40	6.95
	-	1.4	10	250	152.2	200	40	6.8
	-	1.4	10	300	152.2	200	40	6.4
	-	1.4	10	50	152.2	200	50	4.55
	-	1.4	10	100	152.2	200	50	7.1
	-	1.4	10	150	152.2	200	50	7.78
	-	1.4	10	200	152.2	200	50	7.65
	-	1.4	10	250	152.2	200	50	6.8
	-	1.4	10	300	152.2	200	50	7.25
	-	1.4	30	50	152.2	200	30	9.3
	-	1.4	30	100	152.2	200	30	16.25
[57]	-	1.4	30	150	152.2	200	30	16.2
	-	1.4	30	200	152.2	200	30	22.1
	-	1.4	30	250	152.2	200	30	15.6
	-	1.4	30	300	152.2	200	30	15.85
	-	1.4	30	50	152.2	200	40	9.15
	-	1.4	30	100	152.2	200	40	14.9
	-	1.4	30	150	152.2	200	40	16.05
	-	1.4	30	200	152.2	200	40	16.15
	-	1.4	30	250	152.2	200	40	16.11
	-	1.4	30	300	152.2	200	40	16.9
	-	1.4	30	100	152.2	200	50	17.8
	-	1.4	30	150	152.2	200	50	15.22
	-	1.4	30	200	152.2	200	50	18.5
	-	1.4	30	250	152.2	200	50	19
	-	1.4	30	300	152.2	200	50	17.71
	-	1.4	50	50	152.2	200	30	13.3
	-	1.4	50	100	152.2	200	30	26

Table A1. *Cont.*

References	Specimen Label	t_f (mm)	b_f (mm)	L_f (mm)	E_f (GPa)	b_c (mm)	f_c (MPa)	P_u (kN)
	-	1.4	50	150	152.2	200	30	27.8
	-	1.4	50	200	152.2	200	30	27.2
	-	1.4	50	250	152.2	200	30	24.84
	-	1.4	50	300	152.2	200	30	23
	-	1.4	50	100	152.2	200	40	24.5
	-	1.4	50	150	152.2	200	40	27.75
	-	1.4	50	200	152.2	200	40	19.3
	-	1.4	50	250	152.2	200	40	21.9
	-	1.4	50	300	152.2	200	40	27.3
	-	1.4	50	100	152.2	200	50	16
	-	1.4	50	150	152.2	200	50	21.25
	-	1.4	50	200	152.2	200	50	25
	-	1.4	50	250	152.2	200	50	24.9
	-	1.4	50	300	152.2	200	50	34
	T1a	0.352	100	60	209	140	55.6	20
	T1b	0.352	100	60	209	140	55.6	18.8
	T2a	0.352	100	80	209	140	55.6	25.8
	T2b	0.352	100	80	209	140	55.6	25.2
	T3a	0.352	100	100	209	140	55.6	25.8
	T3b	0.352	100	100	209	140	55.6	27.3
	T4a	0.352	100	140	209	140	55.6	26.7
	T4b	0.352	100	140	209	140	55.6	25.9
	T5a	0.352	100	180	209	140	55.6	27.8
	T5b	0.352	100	180	209	140	55.6	31.7
	T6a	0.352	100	220	209	140	55.6	31.7
	T6b	0.352	100	220	209	140	55.6	28.6
[58]	T7a	0.352	100	100	209	140	55.6	33
	T7b	0.352	100	100	209	140	55.6	26.9
	T8a	0.352	100	100	209	140	55.6	28.5
	T8b	0.352	100	100	209	140	55.6	29.8
	T9a	1.056	100	100	209	140	55.6	28.4
	T9b	1.056	100	100	209	140	55.6	29.8
	T10a	1.056	100	140	209	140	55.6	37.4
	T10b	1.056	100	140	209	140	55.6	33.3
	T11a	1.056	100	180	209	140	55.6	42.8
	T11b	1.056	100	180	209	140	55.6	39
	T12a	0.352	70	100	209	140	55.6	21.1
	T12b	0.352	70	100	209	140	55.6	24.2
	C150_1	0.165	100	150	230	150	35	18.97
	C150_2	0.165	100	150	230	150	35	16.51
	C150_3	0.165	100	150	230	150	35	14.26
	C100_1	0.165	100	100	230	150	35	13.63
	C100_2	0.165	100	100	230	150	35	13.36
	C100a_1	0.33	50	150	230	150	35	15.24
	C100a_2	0.33	50	150	230	150	35	18.19
	C100a_3	0.33	50	150	230	150	35	20.53
	C100a_4	0.165	100	150	230	150	35	19.5
	C-60-1	1.3	60	300	175	160	19	19.5
	C-602	1.3	60	300	175	160	19	19.5
	C-60-3	1.3	60	300	175	160	19	19.5
[59]	C-100-1	1.6	100	300	109	160	19	19.5
	C-100-2	1.6	100	300	109	160	19	19.5
	C-100-3	1.6	100	300	109	160	19	19.5
	C-100-4	1.2	100	300	166	160	19	19.5

Table A1. *Cont.*

References	Specimen Label	t_f (mm)	b_f (mm)	L_f (mm)	E_f (GPa)	b_c (mm)	f_c (MPa)	P_u (kN)
[60,61]	C-1.3 × 60-1	1.3	60	300	175	160	19	33.18
	C-1.3 × 60-2	1.3	60	300	175	160	19	29.86
	C-1.3 × 60-3	1.3	60	300	175	160	19	31.88
	C-1.6 × 100-1	1.6	100	300	109	160	19	41.41
	C-1.6 × 100-2	1.6	100	300	109	160	19	39.87
	C-1.6 × 100-3	1.6	100	300	109	160	19	47.72
	C-1.2 × 100-1	1.2	100	300	166	160	19	49.85
	C-1.2 × 100-2	1.2	100	300	166	160	19	48.08
	C-1.2 × 100-3	1.2	100	300	166	160	19	52.6
	C-1.25 × 100-1	1.25	100	300	171	160	19	41.25
	C-1.25 × 100-2	1.25	100	300	171	160	19	38.14
	C-1.25 × 100-3	1.25	100	300	171	160	19	32.68
	C-1.7 × 100-1	1.7	100	300	221	160	19	54.79
	C-1.7 × 100-2	1.7	100	300	221	160	19	51.41
	C-1.7 × 100-3	1.7	100	300	221	160	19	54.57
	5 (25)	1.4	50	250	140	150	37.55	39.78
	11 (25)	1.4	50	250	140	150	35.7	31
	17 (25)	1.4	50	200	140	150	32.78	35.65
[62]	-	1.02	25	203	108.38	228.6	36.4	11.57
	-	1.2	50	400	165	150	52.6	23
	-	1.2	80	400	165	150	52.6	36.75
	-	1.2	50	200	165	150	52.6	19.8
	-	1.2	80	200	165	150	52.6	33
	-	1.2	80	355	195.7	150	52.6	34.5
	-	1.2	80	355	195.7	150	52.6	33.5
	-	1.2	80	355	197.63	150	52.6	37.6
	-	1.2	80	355	197.63	150	52.6	39.1
	-	1.2	80	355	195.46	150	52.6	41
	-	1.2	80	355	195.46	150	52.6	38
	-	0.13	80	355	283.653	150	52.6	16.5
	-	0.13	80	355	283.653	150	52.6	17.4
	-	0.13	80	355	291.024	150	52.6	14.4
	-	0.13	80	355	291.024	150	52.6	14.6
	V12A	1.2	80	400	180	150	26	40
	V9A	1.2	80	400	180	150	26	37
	V13A	1.2	80	400	180	150	26	37.5
	V16A	0.166	100	400	241	150	26	25.1
	V14A	0.166	100	400	241	150	26	24.27
	V17A	0.166	100	400	241	150	26	25.19
	V14B	0.166	100	100	241	150	26	27
	V16B	0.166	100	100	241	150	26	21
	V15B	0.166	100	100	241	150	26	21.5
	V11A	1.2	80	400	180	150	26	32.77
	V7A	1.2	80	400	180	150	26	35.01
	V8A	1.2	80	400	180	150	26	29.15
	V24A	0.166	100	400	241	150	26	25.39
	V26A	0.166	100	400	241	150	26	21.71
	V25A	0.166	100	400	241	150	26	29.09
	V24B	0.166	100	100	241	150	26	20.45
	V25B	0.166	100	100	241	150	26	21.22
	V26B	0.166	100	100	241	150	26	21.45
	V21b	0.166	100	400	241	150	26	20.82
	V22b	0.166	100	400	241	150	26	18.97
	V23b	0.166	100	400	241	150	26	20.14
	V21a	0.166	100	100	241	150	26	16.85
	V23a	0.166	100	100	241	150	26	19.4

References

1. Hasan, K.; Salih, Y.; Binici, H.; Erhan, Y.; Nihat, C. May 1, 2003 Turkey-Bingöl earthquake: Damage in reinforced concrete structures. *Eng. Fail. Anal.* **2004**, *11*, 279–291.
2. Funari, M.F.; Verre, S. The Effectiveness of the DIC as a Measurement System in SRG Shear Strengthened Reinforced Concrete Beams. *Crystals* **2021**, *11*, 265. [CrossRef]
3. Funari, M.F.; Spadea, S.; Fabbrocino, F.; Luciano, R. A moving interface finite element formulation to predict dynamic edge debonding in FRP-strengthened concrete beams in service conditions. *Fibers* **2020**, *8*, 42. [CrossRef]
4. Aiello, M.A.; Leone, M. Interface analysis between FRP EBR system and concrete. *Compos. Part B Eng.* **2008**, *39*, 618–626. [CrossRef]
5. Leone, M.; Sciolti, M.S.; Aiello, M.A. Analysis of the Interface Performance of Concrete Elements Reinforced with Synthetic, Natural and Steel FRP Materials. In Proceedings of the 4th International Symposium on Bond in Concrete 2012: Bond Anchorage, Detailing, Volume 2: Bond in Concrete 2012: Bond in New Materials and under Severe Conditions, Brescia, Italy, 17–20 June 2012; ISBN 978-88-907078-3-4.
6. Teng, J.G.; Smith, S.T.; Yao, J.; Chen, J.F. Intermediate crack-induced debonding in RC beams and slabs. *Constr. Build. Mater.* **2003**, *17*, 447–462. [CrossRef]
7. Savoia, M.; Ferracuti, B.; Mazzotti, C. Non-linear bond slip law for FRP-concrete interface. In Proceedings of the FRPRCS-6, Singapore, 8–10 July 2003.
8. Ulaga, T.; Vogel, T. Bilinear stress-slip bond model: Theoretical background and significance. In Proceedings of the FRPRCS-6, Singapore, 8–10 July 2003.
9. Dai, J.G.; Ueda, T. Local bond stress slip relations for FRP sheets-concrete interfaces. In Proceedings of the FRPRCS-6, Singapore, 8–10 July 2003.
10. Chen, J.F.; Teng, J.G. Anchorage strength models for FRP and steel plates bonded to concrete. *J. Struct. Eng. ASCE* **2001**, *127*, 784–791. [CrossRef]
11. Wu, Z.S.; Yuan, H.; Niu, H.D. Stress transfer and fracture propagation in different kinds of adhesive joints. *J. Eng. Mech. ASCE* **2002**, *128*, 562–573. [CrossRef]
12. Yuan, H.; Teng, J.G.; Seracino, R.; Wu, Z.S.; Yao, J. Full-range behaviour of FRP-to-concrete bonded joints. *Eng. Struct.* **2004**, *26*, 553–565. [CrossRef]
13. Yao, J.; Teng, J.G.; Chen, J.F. Experimental study on FRP-to-concrete bonded joints. *Compos. Part B Eng.* **2005**, *36*, 99–113. [CrossRef]
14. Czaderski, C. Strengthening of reinforced concrete members by pre-stressed, externally bonded reinforcement with gradient anchorage. Ph.D. Thesis, ETH, Zurich, Switzerland, 2012. Available online: http://dx.doi.org/10.3929/ethz-a-007569614 (accessed on 5 June 2021).
15. Ceroni, F.; Barros, J.; Pecce, M.; Ianniciello, M. Assessment of nonlinear laws for near-surface-mounted system in concrete elements. *Compos. Part B Eng.* **2013**, *45*, 666–681. [CrossRef]
16. Lua, X.Z.; Ye, L.P.; Teng, J.G.; Jianga, J.J. Meso-scale finite element model for FRP sheets/plates bonded to concrete. *Eng. Struct.* **2005**, *27*, 564–575. [CrossRef]
17. Lu, X.Z.; Jiang, J.J.; Teng, J.G.; Ye, L.P. Finite element simulation of debonding in FRP-to-concrete bonded joints. *Constr. Build. Mater.* **2006**, *20*, 412–424. [CrossRef]
18. Sümer, Y.; Aktaş, M. Bond length effect of fiber reinforced polymers bonded reinforced concrete beams. *Int. J. Phys. Sci.* **2011**, *6*, 5795–5803.
19. Atheer, F.; Al-Saoudi; Kalfat, R.; Al-Mahaidi, R. Finite Element Assessment on Bond Behavior of FRP-to-Concrete Joints under Cyclic Loading. *Int. J. Civ. Environ. Struct. Constr. Archit. Eng.* **2015**; 9, 1610–1615.
20. Smith, S.T.; Teng, J.G.; Lu, M. Neural Network prediction of plate end debonding in FRP-plated RC beams. In Proceedings of the FRPRCS-6, Singapore, 8–10 July 2003.
21. Ghen, J.F.; Yang, Z.J.; Holt, G.D. FRP or steel plate-to-concrete bonded joints: Effect of test methods on experimental bond strength. *Steel Compos. Struct.* **2001**, *1*, 231–244.
22. Van Gemert, D. Force transfer in epoxy bonded steel/concrete joints. *Int. J. Adhes. Adhes.* **1980**, *1*, 67–72. [CrossRef]
23. Holzenkämpfer, P. Ingenieur Modelle des Verbundes Geklebter Bewehrung für Betonbauteile. Ph.D. Thesis, TU Braunschweig, Brunswick, Germany, 1994. (In German)
24. Tanaka, T. Shear Resisting Mechanism of Reinforced Concrete Beams with CFS as Shear Reinforcement. Master's Thesis, Hokkaido University, Hokkaido, Japan, 1996.
25. Hiroyuki, Y.; Wu, Z.S. Analysis of debonding fracture properties of CFS strengthened member subject to tension. In Proceedings of the 3rd International Symposium on Non-Metallic (FRP) Reinforcement for Concrete Structures, Sapporo, Japan, 14–16 October 1997; Japan Concrete Institute: Tokyo, Japan, 1997; Volume 1, pp. 287–294.
26. Maeda, T.; Asano, Y.; Sato, Y.; Ueda, T.; Kakuta, Y. A study on bond by mechanism of carbon fiber sheet. In Proceedings of the 3rd International Symposium on Non-metallic (FRP) Reinforcement for Concrete Structures, Sapporo, Japan, 14–16 October 1997; Japan Concrete Institute: Tokyo, Japan, 1997; Volume 1, pp. 279–286.
27. Khalifa, A.; Gold, W.J.; Nanni, A.; Abdel Aziz, M. Contribution of externally bonded FRP to shear capacity of flexural members. *J. Compos. Constr.* **1998**, *2*, 195–203. [CrossRef]

28. Niedermeier, R. Envelope line of tensile forces while using externally bonded reinforcement. Ph.D. Thesis, TU München, Munich, Germany, 2000. (In German)

29. Singh, A.; del Rey Castillo, E.; Ingham, J. FRP-to-FRP bond characterization and force-based bond length model. *Compos. Struct.* **2019**, *210*, 724–734. [CrossRef]

30. fib. *Externally Bonded FRP Reinforcement for RC Structures. Design and Use of Externally Bonded Fiber Reinforced Polymer Reinforcement (FRP EBR) for Reinforced Concrete Structures*; fib Bulletin 14. Task Group 9.3; FRP Reinforcement for Concrete Structures; fib: Lausanne, Switzerland, 2001.

31. Yang, Y.X.; Yue, Q.R.; Hu, Y.C. Experimental study on bond performance between carbon fiber sheets and concrete. *J. Build. Struct.* **2001**, *22*, 36–42.

32. Japan Concrete Institute (JCI). Technical report of technical committee on retrofit technology. In Proceedings of the International Symposium on Latest Achievement of Technology and Research on Retrofitting Concrete Structures, Kyoto, Japan, 14–15 July 2003; Japan Concrete Institute (JCI): Tokyo, Japan, 2003.

33. SIA 166. *Kelebebewehrungen (Externally Bonded Reinforcement)*; Schweizerichenr Ingegneur-und Architektenveirein SIA: Zurich, Switzerland, 2004.

34. Dai, J.; Ueda, T.; Sato, Y. Development of the nonlinear bond stress–slip model of fiber reinforced plastics sheet–concrete interfaces with a simple method. *J. Compos. Constr.* **2005**, *9*, 52–62. [CrossRef]

35. Lu, X.Z.; Teng, J.G.; Ye, L.P.; Jiang, J.J. Bond-slip models for FRP sheets/plates bonded to concrete. *J. Eng. Struct.* **2005**, *27*, 920–937. [CrossRef]

36. Wu, Z.S.; Islam, S.M.; Said, H. A three-parameter bond strength model for FRP–concrete interface. *J. Reinf. Plast. Compos.* **2009**, *28*, 2309–2323. [CrossRef]

37. Wu, Y.; Zhou, Z.; Yang, Q.; Chen, W. On shear bond strength of FRP-concrete structures. *J. Eng. Struct.* **2010**, *32*, 897–905. [CrossRef]

38. *TR 55 Design Guidance for Strengthening Concrete Structures Using Fibre Composite Materials*, 3rd ed.; Concrete Society: Camberley, UK, 2012.

39. CNR-DT 200 R1/2013. *Istruzioni per la Progettazione, l'Esecuzione ed il Controllo di Interventi di Consolidamento Statico mediante l'utilizzo di Compositi Fibrorinforzati*; Concilio Nazionale delle Ricerche: Roma, Italy, 2013. (In Italian)

40. Alqedra, M.A.; Ashour, A.F. Prediction of shear capacity of single anchors located near a concrete edge using neural networks. *Comput. Struct.* **2005**, *83*, 2495–2502. [CrossRef]

41. Dahou, Z.; Sbartai, Z.M.; Caste, A.; Ghomari, F. Artificial neural network for steel-concrete bond prediction. *Eng. Struct.* **2009**, *31*, 1724–1733. [CrossRef]

42. Tinoco, J.; Correia, A.G.; Cortez, P. Application of data mining techniques in the estimation of the uniaxial compressive strength of jet grouting columns over time. *Constr. Build. Mater.* **2011**, *25*, 1257–1262. [CrossRef]

43. Amani, J.; Moeini, R. Prediction of shear strength of reinforced concrete beams using adaptive neuro-fuzzy inference system and artificial neural network. *Sci. Iran. A* **2012**, *19*, 242–248. [CrossRef]

44. Yousif, S.T. New model of CRFP-confined circular concrete columns: ANN approach. *Int. J. Civ. Eng. Technol.* **2013**, *4*, 98–110.

45. Cascardi, A.; Micelli, F.; Aiello, M.A. Analytical model based on artificial neural network for masonry shear walls strengthened with FRM systems. *Compos. Part B Eng.* **2016**, *95*, 252–263. [CrossRef]

46. Cascardi, A.; Micelli, F.; Aiello, M.A. An Artificial Neural Networks model for the prediction of the compressive strength of FRP-confined concrete circular columns. *Eng. Struct.* **2017**, *140*, 199–208. [CrossRef]

47. Chajes, M.J.; Finch, W.W.; Januszka, T.F.; Thonson, T.A. Bond and force transfer of composite material plates bonded to concrete. *ACI Struct. J.* **1996**, *93*, 209–217.

48. Takeo, K.; Matstushiba, H.; Makizumi, T.; Nagashima, G. Bond characteristics of CFRP sheets in the CFRP bonding technique. *Proc. Japan Concr. Inst.* **1997**, *19*, 1599–1604.

49. Yao, J. Debonding Failures in Reinforced Concrete Structures Strengthened with Externally Bonded FRP Sheets/Plates. Ph.D. Thesis, Hong Kong Polytechnic University, Hong Kong, 2004.

50. Toutanji, H.; Saxena, P.; Zhao, L.Y.; Ooi, T. Prediction of interfacial bond failure of FRP-concrete surface. *J. Compos. Constr.* **2007**, *11*, 427–436. [CrossRef]

51. Tan, Z. Experimental Research for RC Beam Strengthened with GFRP. Master's Thesis, Tsinghua University, Beijing, China, 2002.

52. Zhao, H.D.; Zhang, Y.; Zhao, M. Research on the bond performance between CFRP plate and concrete. In Proceedings of the 1st Conference on FRP-Concrete Structures of China; 2000; pp. 247–253.

53. Ren, H.T. Study on Basic Theories and Long-Time Behavior of Concrete Structures Strengthened by Fiber Reinforced Polymers. Master's Thesis, Dalian University of Technology, Dalian, China, 2003. (In Chinese).

54. Ueda, T.; Sato, Y.; Asano, Y. Experimental study on bond strength of continuous carbon fiber sheet. *Spec. Publ.* **1999**, *188*, 407–416.

55. Wu, Z.S.; Yuan, H.; Hiroyuki, Y.; Toshiyuki, K. Experimental/analytical study on interfacial fracture energy and fracture propagation along FRP-concrete interface. *Spec. Publ.* **2001**, *201*, 133–152.

56. Sharma, S.K.; Mohamed, M.S.; Goldar, D.; Sikdar, P.K. Plate–concrete interfacial bond strength of FRP and metallic plated concrete specimens. *J. Compos. Part B Eng.* **2006**, *37*, 54–63. [CrossRef]

57. Woo, S.K.; Lee, Y. Experimental study on interfacial behavior of CFRP-bonded concrete. *J. Civil. Eng.* **2010**, *14*, 385–393. [CrossRef]

58. Pham, H.B.; Al-Mahaidi, R. Modelling of CFRP-concrete shear-lap test. *Constr. Build. Mater.* **2005**, *21*, 727–735. [CrossRef]

59. Ceroni, F.; Pecce, M. Bond performance in concrete elements strengthened with CFRP sheets. In Proceedings of the FRP RCS8, Patras, Greece, 16–18 July 2007.
60. Mazzotti, C.; Ferracuti, B.; Bilotta, A.; Ceroni, F.; Nigro, E.; Pecce, M. Sensitivity of FRP-concrete bond behavior to modification of the experimental set-up. In Proceedings of the International Conference on FRP Composites in Civil Engineering-CICE 2012, Rome, Italy, 13–15 June 2012.
61. Bilotta, A.; Ceroni, F.; Di Ludovico, M.; Nigro, E.; Pecce, M.; Manfredi, G. Bond efficiency of EBR and NSM FRP systems for strengthening of concrete members. *J. Compos. Constr.* **2011**. [CrossRef]
62. Faella, C.; Nigro, E.; Martinelli, E.; Sabatino, M.; Salerno, N.; Mantegazza, G. Aderenza tra calcestruzzo e Lamine di FRP utilizzate come placcaggio di elementi inflessi. Parte I: Risultati sperimentali. In Proceedings of the XIV Congresso, C.T.E., Mantova, Italy, 7–8 November 2002. (In Italian).
63. Ferracuti, B. Strengthening of RC Structures by FRP: Experimental Analyses and Numerical Modelling. Ph.D. Thesis, University of Bologna, Bologna, Italy, 2006.
64. Savoia, M.; Bilotta, A.; Ceroni, F.; Di Ludovico, M.; Fava, G.; Ferracuti, B. Experimental round robin test on FRP-concrete bonding. In Proceedings of the 9th International Symposium on Fiber Reinforced Polymer Reinforcement for Concrete Structures, Sydney, Australia, 13–15 July 2009.
65. Czaderski, C.; Soudki, K.; Motavalli, M. Front and side view image correlation measurements on FRP to concrete pull-off bond tests. *J. Compos. Constr.* **2010**, *14*, 451–463. [CrossRef]
66. Haddad, R.H.; Al-Rousan, R.; Almasry, A. Bond-slip behavior between carbon fiber reinforced polymer sheets and heat-damaged concrete. *Compos. Part B Eng.* **2013**, *45*, 1049–1060. [CrossRef]
67. Zhu, H.; Wu, G.; Shi, J.; Liu, C.; He, X. Digital image correlation measurement of the bond–slip relationship between fiber-reinforced polymer sheets and concrete substrate. *J. Reinf. Plast. Compos.* **2014**, *33*, 1590–1603. [CrossRef]
68. McSweeney, B.M.; Lopez, M.M. FRP-concrete bond behavior: A parametric study through pull-off testing. *Spec. Publ.* **2005**, *230*, 441–460.
69. Joanes, D.N.; Gill, C.A. Comparing measures of sample skewness and kurtosis. *J. R. Stat. Soc. (Ser. D) Stat.* **1998**, *47*, 183–189. [CrossRef]
70. Iorfida, A.; Verre, S.; Candamano, S.; Ombres, L. Tensile and direct shear responses of basalt-fibre reinforced mortar-based materials. *Int. Conf. Strain Hardening Cem. Based Compos.* **2018**. [CrossRef]
71. Ombres, L.; Mancuso, N.; Mazzuca, S.; Verre, S. Bond between carbon fabric-reinforced cementitious matrix and masonry substrate. *J. Mater. Civ. Eng.* **2019**, *31*. [CrossRef]
72. Longo, F.; Cascardi, A.; Lassandro, P.; Aiello, M.A. A new Fabric Reinforced Geopolymer Mortar (FRGM) with mechanical and energy benefits. *Fibers* **2020**, *8*, 49. [CrossRef]
73. Cascardi, A.; Longo, F.; Micelli, F.; Aiello, M.A. Compressive strength of confined column with Fiber Reinforced Mortar (FRM): New design-oriented-models. *Constr. Build. Mater.* **2017**, *156*, 387–401. [CrossRef]
74. Cascardi, A.; Micelli, F.; Aiello, M.A. FRCM-confined masonry columns: Experimental investigation on the effect of the inorganic matrix properties. *Constr. Build. Mater.* **2018**, *186*, 811–825. [CrossRef]